Title: An iPSC model of fragile X syndrome reflects clinical phenotypes and reveals m^{6}A-mediated epi-transcriptomic dysregulation underlying synaptic dysfunction

Lu Lu[1,2]*, Avijite Kumer Sarkar[1,2]*, Lan Dao[1,2], Yanchen Liu[3], Chunlong Ma[4], Phyo Han Thwin[4], Xuyao Chang[1,2], George Yoshida[1,2], Annie Li[1], Cenjing Wang[1], Crace Westerkamp[3], Lauren Schmitt[3], Maag Chelsey[5], Monzon Stephanie[5], Yu Zhao[6], Yaping Liu[5], Xiong Wang[7], Ling-Qiang Zhu[8], Dan Liu[8], Jason Tchieu[1,2], Makoto Miyakoshi[3], Haining Zhu[4], Christina Gross[9], Ernest Pedapati[3], Nathan Salomonis[10], Craig Erickson[3], Ziyuan Guo[1,2#]

1. Center for Stem Cell and Organoid Medicine (CuSTOM), Division of Developmental Biology, Cincinnati Children's Hospital Medical Center, Cincinnati, OH 45229, USA;
2. Department of Pediatrics, University of Cincinnati, College of Medicine, Cincinnati, OH 45229, USA;
3. Division of Child and Adolescent Psychiatry, Cincinnati Children's Hospital Medical Center, Cincinnati, OH 45229, USA;
4. Department of Pharmacology and Toxicology, R. Ken Coit College of Pharmacy, University of Arizona, AZ 85721, USA;
5. Division of Human Genetics, Cincinnati Children's Hospital Medical Center, Cincinnati, OH 45229, USA;
6. Department of Computer Science, University of Cincinnati, Cincinnati, OH 45221, USA.
7. Department of Laboratory Medicine, Tongji Hospital, Tongji Medical College, Huazhong University of Science and Technology, Wuhan, China;
8. Department of Pathophysiology, Key Lab of Neurological Disorder of Education Ministry, School of Basic Medicine, Tongji Medical College, Huazhong University of Science and Technology, Wuhan, Hubei, China;
9. Division of Neurology, Cincinnati Children's Hospital Medical Center, Cincinnati, OH 45229, USA;
10. Division of Biomedical Informatics, Cincinnati Children's Hospital Medical Center, Cincinnati, OH 45229, USA.

*These authors contributed equally to this work

Correspondence should be addressed to Ziyuan Guo (Ziyuan.Guo@cchmc.org)

33 Leading contact: Ziyuan Guo, Division of Developmental Biology, Department of Pediatrics,
34 Cincinnati Children's Hospital Medical Center, 3333 Burnet Avenue, Cincinnati, OH 45229, USA.
35 Tel: 513-517-7092, Email: Ziyuan.Guo@cchmc.org.
36
37 **Declaration of interests:** The authors have declared no conflicts of interest.

Abstract

Fragile X syndrome (FXS), the leading genetic cause of intellectual disability, arises from *FMR1* gene silencing and loss of the FMRP protein. N6-methyladenosine (m^6A) is a prevalent mRNA modification essential for post-transcriptional regulation. FMRP is known to bind to and regulate the stability of m^6A-containing transcripts. However, how loss of FMRP impacts on transcriptome-wide m^6A modifications in FXS patients remains unknown. To answer this question, we generated cortical neurons differentiated from induced pluripotent stem cells (iPSC) derived from healthy subjects and FXS patients. In electrophysiology recordings, we validated that synaptic and neuronal network defects in iPSC-derived FXS neurons corresponded to the clinical EEG data of the patients from which the corresponding iPSC line was derived. In analysis of transcriptome-wide methylation, we show that FMRP deficiency led to increased translation of m^6A writers, resulting in hypermethylation that primarily affecting synapse-associated transcripts and increased mRNA decay. Conversely, in the presence of an m^6A writer inhibitor, synaptic defects in FXS neurons were rescued. Taken together, our findings uncover that an FMRP-dependent epi-transcriptomic mechanism contributes to FXS pathogenesis by disrupting m^6A modifications in FXS, suggesting a promising avenue for m^6A-targeted therapies.

Introduction

Fragile X syndrome (FXS) is the most common inherited cause of intellectual disability, and as it often co-occurs with autism spectrum disorders (ASD), is believed to make genetic contributions to both. The syndrome manifests as a spectrum of cognitive impairments and socio-emotional deficits. FXS is primarily caused by the presence of expanded trinucleotide repeats in the fragile X messenger ribonucleoprotein 1 (*FMR1*) gene, leading to transcriptional silencing and consequent loss of Fragile X mental retardation protein (FMRP). With excessive glutamatergic signaling a pathological hallmark of FXS, previous research primarily focused on excitatory synaptic transmission, and in particular signaling downstream of the metabotropic glutamate receptor subtype 5 (mGluR5) [1,2]. However, given the limited success of mGluR5-targeted therapies, the focus has shifted towards assessing how the balance between excitatory and inhibitory (E/I) signaling impact on network hyperexcitability [3-6]. Despite insights gained from FMRP loss-of-function studies in animal models, clinical trials for FXS, while showing promise in preclinical studies, have yielded limited success [7,8]. More recently, advancements have been made in modeling FXS using patient-derived induced pluripotent stem cells (iPSCs) [9-14], which mirror neurodevelopmental and synaptic abnormalities within the human cellular and genetic

context. However, the extent to which human cultured neurons faithfully recapitulate FXS-associated disease phenotypes *in vitro* and in a way that could inform development of therapeutic strategies remains uncertain. Consequently, bridging the gap between experimental models and human disease holds paramount importance in advancing FXS research.

N6-methyladenosine (m^6A) is a prevalent RNA modification in mammalian messenger RNAs (mRNAs). It is installed by 'writers' (known as methyltransferases) like the METTL3/14 complex, including METTL3, METTL14, and WTAP[15-20], and removed by 'erasers' such as Fat Mass and Obesity-Associated Protein (FTO) and AlkB Homolog 5 (ALKBH5) [20-22]. The m^6A modification instructs regulation of RNA processes such as splicing, export, translation, and decay through the actions of m^6A 'readers' that bind m^6A-marked mRNAs[20,23-25]. In the nervous system, m^6A modifications are particularly abundant and play established roles in brain development and neuronal functions [26-31]. Genome-wide association studies (GWAS) have identified rare and *de novo* variants of the m^6A reader YTHDC2 [32-35] that are strongly associated with ASD (SFARI Gene Score 2). However, our understanding of m^6A regulation in human neurons, especially under pathological conditions, is still in its infancy. Consequently, transcriptome-wide m^6A profiling in patient-derived neurons stands to significantly advance our understanding of how this modification impacts on pathological events and neuronal dysfunction.

FMRP, a multifunctional RNA-binding protein [36] primarily localized to translating polyribosomes, regulates local protein synthesis at synapses [37-39]. Its deficiency results in increased synthesis of synapse-related proteins. Recently identified as a putative m^6A 'reader' via unbiased proteomics studies [40-42], FMRP influences a range of neural processes such as neural progenitor proliferation and differentiation, synaptic transmission, plasticity, and axon growth [43-47]. Despite a conserved consensus sequence between FMRP-binding sites and m^6A methylation, FMRP interacts directly with m^6A 'readers' in an m^6A-modified mRNA-independent manner [46,47] and negatively regulates their functions [45-47]. Specifically, FMRP antagonizes the activity of m^6A readers, YTHDF2 and YTHDF1 (as well as the Drosophila homolog ythdf), stabilizing m^6A-marked mRNAs and controlling their translation [45-47]. However, the precise mechanisms by which FMRP deficiency impacts transcriptome-wide m^6A modifications in patient-derived neurons remains elusive, and especially, to what extent this modification impacts on synaptic and neuronal dysfunction, eventually contributing to FXS pathology.

105 Here, we established a patient-derived iPSC neuron model of FXS and identified an imbalance
106 in excitatory/inhibitory (E/I) signaling, along with hyperexcitability and hyperconnectivity in FXS
107 cortical circuitry, which correlated with each individual's clinical electroencephalogram (EEG)
108 data. Notably, loss of FMRP leads to elevated m^6A levels in both FXS patient-derived neurons
109 and *Fmr1* Knockout mice brains. In mechanistic studies, we uncovered that FMRP deficiency
110 disrupts the translational control of m^6A writer expression, leading to accumulation of excessive
111 m^6A-tagged transcripts related to synapse function in FXS neurons and increased mRNA decay
112 of such synapse-related genes. Conversely, treatment with a m^6A writer inhibitor, capable of
113 reducing excessive m^6A modifications, mitigated synaptic and functional defects in FXS neurons
114 by restoring mRNA stability. Our findings unveil a novel m^6A-mediated epi-transcriptomic
115 mechanism underlying FXS, by which FMRP deficiency leads to increased translation of m^6A
116 writers, resulting in transcriptome-wide hypermethylation and points to potential translational
117 significance of m^6A-modifying drugs as promising therapeutics for FXS treatment.
118
119 **Result**
120 **Modeling FXS using patient-derived iPSCs and cortical neurons**
121 In this study, we enrolled seven individuals with FXS and performed neuropsychological
122 examinations on five of them, documenting significantly lower full-scale intelligence quotient
123 (FSIQ, 45.71 $\pm$ 8, n = 5 FXS subjects), nonverbal IQ (NVIQ, 34.04 $\pm$ 8.95, n = 5 FXS subjects)
124 and verbal IQ (VIQ, 57.38 $\pm$ 8.24, n = 5 FXS subjects), indicative of intellectual disability
125 (Supplemental Table 1). We also validated that FMRP protein levels and FMR1 mRNA levels in
126 blood samples from FXS patients were low or absent (Supplemental Table 1).
127 To model FXS, we generated induced pluripotent stem cells (iPSCs) from these seven
128 FXS patients and age- and gender-matched healthy controls, and confirmed pluripotency,
129 stemness, and karyotype integrity of all the iPSC lines (Supplemental Table 1). We also
130 confirmed via PCR and Asuragen testing that CGG repeat numbers were elevated in FXS
131 patients (over 200 CGG repeats in the 5' UTR of the FMR1 gene compared with 30 or fewer in
132 healthy controls; Supplemental Table 1 and Supplemental Figure 1A). The expression of
133 forebrain cortical neural progenitor markers (Sox2, Nestin, ZO1, FOXG1, OTX2, PAX6) and
134 mature neuronal markers (Tuj1, CaMKII), along with cortical layer markers (BRN2, CTIP2,
135 TBR1), indicated successful induction of neuroepithelial cell fate (Figure 1A, B and
136 Supplemental Figure 1B, C). Importantly, the FXS patient-derived cortical neurons lacked FMRP
137 expression, unlike their control counterparts (Figure 1C, D), replicating a hallmark of FXS
138 pathology.

In western blot and immunostaining analysis, we identified elevated levels of synaptic proteins Synapsin II and SV2 (Figure 1E, F) and an increase in numbers of synaptic puncta (Figure 1G, H) in the FXS cortical neurons. We also detected distinct alterations in spine morphology, including reduced mushroom-like spines and increased numbers of filopodia-like spines compared to control neurons (Figure 1I-K). However, we did not detect any significant differences in neurites including number of sections, total neurite length, terminal points, branch points, maximum section length, minimum section length, and mean section length between FXS neurons and controls (Supplemental Figure 1D-L). Taken together, these observations align with previous research linking the absence of FMRP to changes in synaptic protein expression and synaptic structure in FXS neurons [10,11,48-51].

Dysregulated synaptic transmission, excitatory/inhibitory imbalance, and hyperexcitability in cortical neurons derived from FXS iPSCs

To delve into the functional aspects of our iPSC model system, we conducted comprehensive electrophysiological analyses, including whole-cell patch-clamp and micro-electrode arrays (MEA). In whole-cell patch-clamp recordings (Figure 2A), we noted a consistent and significant increase in excitatory synaptic transmission in FXS cortical neurons relative to controls (Figure 2B). Specifically, the inter-event interval was decreased in excitatory postsynaptic currents (EPSC) whereas the frequency was elevated but the amplitude reduced (Figure 2C, D). We also observed an overall decrease in inhibitory synaptic transmission in FXS cortical neurons relative to controls (Figure 2E), manifested as an increase in inter-event interval and lower frequency and amplitudes of inhibitory postsynaptic currents (IPSC) (Figure 2F, G).

Beyond the synaptic transmission defects and E/I imbalance, FXS cortical neurons were hyperexcitable, reflected as an increased frequency of evoked action potentials (APs) and decreased thresholds to firing APs (Figure 2I, J). Other parameters, including evoked AP amplitude and Rheobase, remained unchanged (Supplemental Figure 2A, B). Additionally, the frequency of spontaneous AP was higher in FXS cortical neurons relative to control cortical neurons (Figure 2K, L). However, we did not observe any significant disparities in sodium and potassium channel activities between FXS and control neurons (Supplemental Figure 2C-E). Taken together, our data thus far suggested a causal relationship between E/I imbalance and hyperexcitability in FXS iPSC-derived cortical neurons.

Hyperactivity and hyperconnectivity in cortical circuitry derived from FXS iPSCs

172 To monitor cortical circuitry activity, we cultured 0.5 million neurons on a MEA chip with 64
173 electrodes and recorded field potentials for 5 minutes at 4, 5, 6, 7, and 8 weeks (Figure 3A and
174 Supplemental Figure 3A). Data were sampled at 20 kHz with a 1-1000 Hz frequency bandwidth
175 (see Methods). We identified spikes based on a threshold (5.5 times the standard deviation of
176 peak-to-peak noise), and bursts as sequences of at least 3 spikes with inter-spike intervals
177 within 300 milliseconds and a duration exceeding 200 milliseconds. In FXS iPSC-derived
178 cortical circuitry, we found heightened spike and burst activity in sample traces (Figure 3B),
179 characterized by a decreased inter-spike interval, increased burst duration, and more spikes per
180 burst, indicative of hyperactivity (Figure 3C-E).
181 Additionally, analysis of array-wide spike detection rate (ASDR) revealed enhanced
182 neuronal network synchrony and hyperconnectivity in FXS iPSC-derived cortical microcircuitry
183 (Figure 3F), reflected as increased burst peak and duration, more active electrodes per network
184 burst, and elevated spike numbers in network bursts (Figure 3G-J). When sorting spikes for
185 each electrode based on waveforms, we found significantly more waveforms in FXS iPSC-
186 derived cortical microcircuitry (Supplemental Figure 3B, C), indicating more synchronized
187 neurons in FXS cortical circuitry. Lastly, UP-state analysis, associated with synchronized activity
188 across a network of neurons, particularly in the cortex, exhibited longer durations in FXS iPSC-
189 derived cortical circuitry (Figure 3K, L). Taken together, these electrophysiological findings
190 identify both cortical network hyperactivity and hyperconnectivity in the FXS cortical
191 microcircuitry.
192 To bridge the gap between *in vitro* models and patients, we examined
193 electroencephalogram (EEG) recordings from the same individuals and correlated these with
194 clinical neuropsychological symptoms. We had already noted deviations in FSIQ, NVIQ, and
195 VIQ in FXS subjects as indications of intellectual disabilities (Supplemental Table 1).
196 Additionally, we assessed the absolute neural power spectral densities (PSDs) of typically
197 developing control (TDC) and FXS EEG data (Supplemental Figure 3D). We found high gamma
198 power in FXS subjects (Figure 3M), which is associated with hyperactivity and inversely
199 correlated with NVIQ in FXS subjects [52-55]. Using FOOOF (Fitting Oscillations and One-Over-F)
200 analysis to parameterize the PSDs [56,57], we found that the FOOOF slope was higher in FXS
201 subjects (Figure 3N), an additional indication of cortical hyperactivity and hyperconnectivity.
202 Taken together, these findings strongly suggest that key pathophysiological signatures in FXS
203 patients such as cortical hyperactivity and hyperconnectivity can be modeled in patient-derived
204 neurons, underscoring the translational potential and clinical relevance of our human model
205 system in uncovering disease-related mechanisms.

206

207 **FMRP-bound mRNAs encoding m^{6}A writers and FMRP deficiency increasing writer**
208 **expression**

209 Like FMRP, the mRNA modification m^{6}A is highly enriched in the brain, where it plays a crucial
210 role in neurodevelopment and in mature neurons [26-31]. To quantify total m^{6}A levels, we purified
211 mRNAs and conducted dot plot analysis using an anti-m^{6}A antibody to detect m^{6}A tag-tagged
212 mRNAs. Relative to control, m^{6}A levels were notably increased in FXS iPSC-derived cortical
213 neurons (Figure 4A). Additionally, we found increased protein, but not mRNA, expression of m^{6}A
214 writers, including METTL3, METTL14, and WTAP, the key METTL3/14 complex components
215 (Figure 4B-D). We documented similar findings in *Fmr1* knockout mice (Supplemental Figure 4).
216 These findings suggest that FMRP deficiency leads to elevated m^{6}A levels through upregulation
217 of m^{6}A writer protein expression.

218 To determine whether FMRP binds mRNAs encoding m^{6}A writers, we transfected HEK293T
219 cells with flag-mCherry-FMRP and flag-mCherry plasmids, and conducted pulldown using anti-
220 flag M2 affinity gel (Figure 4E) [58]. In the pulldowns with flag-tagged mCherry-FMRP, but not with
221 flag-tagged mCherry, we observed significant enrichment of METTL3, METTL14, and WTAP
222 mRNAs (Figure 4F). There was no specific enrichment for GAPDH mRNAs, indicating that FMRP
223 binds METTL3, METTL14, and WTAP mRNAs. To investigate whether FMRP regulates
224 translation of the m^{6}A writer translation, we analyzed the translationally active heavy polysome
225 fractions (see Methods)[59]. Indeed, in FXS patient-derived neurons, METTL3, METTL14, and
226 WTAP were all significantly enriched in the heavy polysome fraction (Figure 4G). In addition, the
227 overall protein translation efficiency increased by 23.5% in FXS neurons (Figure 4H). These
228 findings suggest that basal translation of m^{6}A writer mRNAs is enhanced in the absence of FMRP.

229

230 **Transcriptome-wide m^{6}A dysregulation in cortical neurons derived from FXS iPSCs**

231 As a comprehensive profiling of transcriptome-wide m^{6}A modifications in the context of FXS
232 remains outstanding, we next performed methylated RNA immunoprecipitation sequencing
233 (MeRIP-Seq) of neurons derived from six FXS patients and seven control samples (see
234 Methods). When comparing datasets, we identified 3,313 m^{6}A-enriched genes in FXS patient-
235 derived neurons and 2,815 enriched genes in controls, with a widespread distribution across all
236 chromosomes (Figure 5A). This data set indicates a transcriptome-wide neuronal dysregulation
237 of m^{6}A modifications in patients with FXS. Motif analysis and the distribution of m^{6}A peaks
238 confirmed the robustness of MeRIP-Seq and m^{6}A analysis, with a predominant GGAC motif
239 near the stop codon (Figure 5B, C). For benchmarking, we conducted MeRIP-Seq on

postmortem cortex tissues derived from FXS subjects and healthy controls (Supplemental Table 2), and validated motif analysis and m^6A peak distributions, (Supplemental Figure 5A-C). Notably, we identified over 9,000 dys-methylated sites between controls and FXS neurons (Figure 5D) and over 4,000 dys-methylated sites between control and FXS postmortem cortex tissues (Supplemental Figure 5D), indicating transcriptome-wide m^6A dysregulation in cultured FXS neurons and in brain tissues. Interestingly, the majority of genes exhibited one hyper- or hypo-methylation site across all chromosomes (Figure 5 E, F and Supplemental Figure 5E, F).

When we conducted gene ontology (GO) analysis, we identified significant enrichment of genes with elevated m^6A modifications in categories related to synaptic assembly, structure, and function (Figure 5G and Supplemental Figure 5G). Examples include hypermethylation of genes encoding synaptic proteins, such as SYT3 and SYT5, in exons near the stop codon and 3' UTR (Figure 5H). Notably, genes with elevated m^6A modifications overlapped significantly with previously identified FMRP target genes [38], autism-associated genes from the SFARI database, and synapse-related genes from the SynGO database (Figure 5I-K and Supplemental Figure 5H-J). These data underscore the critical role of excessive m^6A tagging in FXS pathologies, particularly synaptic defects, and its broader implications for autism-spectrum disorders. Furthermore, the prominent overlap between hypermethylated genes and FMRP targets, as well as autism-associated genes, was strongly linked to synapse assembly and function (Figure 5L, M and Supplemental Figure 5K, L), reinforcing that dysregulated m^6A modifications and synaptic dysfunction are central to FXS and autism-spectrum disorders.

Dysregulated synapse-related gene expression

We next performed RNA sequencing (RNA-seq) on iPSC-derived neurons from seven healthy controls and six FXS patients (see Methods) and identified over 2,000 significantly differentially expressed genes (DEGs) (Figure 6A). Among these, FMR1 was prominently silenced in FXS iPSC-derived neurons (Figure 6B), consistent with full mutation status (Supplemental Table 1) and loss of FMRP expression (Figure 1C, D). Through functional enrichment analysis, we identified that nearly all top DEGs categories were linked to synaptic structure and function (Figure 6C). Moreover, DEGs significantly overlapped with FMRP target genes, particularly those associated with synapse-related categories and previously reported synapse-related genes (Supplemental Figure 6A-C). These findings highlight gene expression alterations driving synaptic defects in our iPSC-derived cortical neuron model. Similarly, RNA-seq analysis of cortical postmortem tissues from three FXS patients and healthy controls identified nearly 1,500 significantly altered genes (Supplemental Figure 6D). These genes overlapped with FMRP

target and autism-associated genes from the SFARI database (Supplemental Figure 6E-I), highlighting that dysregulated synapse-related gene expression serves as a molecular signature of FXS.

Correlation of hypermethylation with gene downregulation and increased mRNA decay

The regulatory impact of m^6A influences RNA fate and function, modulating various aspects of RNA biology [23-25]. However, whether aberrant m^6A modifications are directly linked to gene expression changes in FXS neurons remains unclear. When we integrated the list of dys-methylated genes (DMGs) (Figure 5) with the DEGs (Figure 6), we revealed a strong correlation between hypermethylation and gene downregulation ("hyper-down" pattern), comprising 64.6% of total correlations ($R = -0.47$, $p < 3.55e-53$, Chi-squared test) (Figure 6D) and indicative of a mechanistic link between hypermethylation and reduced gene expression. Similarly, joint analysis of aberrantly methylated genes and DEGs from FXS postmortem tissues also demonstrated a predominant correlation between hypermethylation and gene downregulation ($R = -0.33$, p-value = 1.152e-53, Chi-squared test), with a notable "hyper-down" pattern in quadrant II (72.9% of total correlations) (Supplemental Figure 6J). These genes were significantly enriched in synapse-related categories (Figure 6E and Supplemental Figure 6K), suggesting that mRNA hypermethylation contributes to synaptic defects by modulating the fate of synapse-related mRNAs, in particular accelerating mRNA decay. Indeed, when we measured mRNA decay rates using actinomycin D treatment and gene-specific RT-qPCR (see Methods), we observed accelerated decay of hypermethylated and downregulated synapse-related transcripts (such as STY7) in FXS neurons (Figure 6F, G). These data suggest that hypermethylation drives transcript degradation and gene downregulation in FXS.

m^6A writer inhibitor rescuing synaptic and functional defects in FXS iPSC-derived cortical neurons

Given the overall increase in m^6A levels (Figure 4A), the association of hypermethylated m^6A marks with downregulated synapse-related genes (Figure 6D), and the observed increase in RNA decay for these hypermethylated genes (Figure 6F), we hypothesized that therapeutic intervention with an m^6A writer inhibitor could alleviate synaptic defects in FXS neurons by restoring normal mRNA stability of synapse-related genes. To test this hypothesis, we treated FXS and control neurons with STM-2457, a small-molecule inhibitor targeting METTL3, the catalytic subunit of the METTL3/14 methyltransferase complex [60]. MeRIP-qPCR (see Methods) revealed that excessive m^6A marks from synapse-related transcripts in FXS neurons were

308 reduced in the presence of STM-2457 but not DMSO (Figure 7A). Additionally, STM-2457
309 restored the accelerated mRNA decay of synapse-related genes such as LRRC4B in FXS iPSC-
310 derived neurons to control levels (Figure 7B). Notably, the two-week administration of the m^6A
311 writer inhibitor reduced abnormal synaptic puncta and excitatory transmission, while significantly
312 mitigating hyperexcitability in FXS neurons, without affecting normal neuronal function (Figure
313 7C-H). These findings highlight the critical role of m^6A in FXS synaptic pathology and suggest
314 therapeutic potential of m^6A-modulating drugs in FXS.
315
316 **Discussion**
317 In this report, we successfully generated iPSC lines from FXS patients matched with controls.
318 We also demonstrated that FXS iPSC-derived neurons recapitulate key aspects of FXS
319 pathology, including *FMR1* gene silencing, loss of FMRP, elevated synaptic protein expression,
320 synaptic puncta, and filopodia-like spines, alongside reduced mushroom spines, consistent with
321 previous related research [48]. Relative to previously reported human PSCs model of FXS [9-13], our
322 system is differentiated by several important features. First, beyond general synaptic
323 transmission defects, our model identified an excitatory/inhibitory imbalance in FXS neurons.
324 Secondly, we characterized a disease-related hyperexcitability and hyperconnectivity in FXS
325 cortical circuitry. Finally, and foremost, these cortical hyperexcitability and hyperconnectivity
326 features were confirmed in the same FXS subjects via analysis of their electroencephalogram
327 (EEG) recording. These findings confirm that cortical hyperexcitability and hyperconnectivity are
328 key pathophysiological signatures in FXS subjects that can be modeled in patient iPSC-derived
329 neuronal models, underscoring the translational potential and clinical relevance of our human
330 model system in uncovering disease-related mechanisms. Taken together, our work represents
331 the first clinically relevant human neuron model for FXS.
332
333 In the mammalian brain, m^6A modifications are prevalent mRNA modifications[23-25], known for
334 their roles in brain development and neuronal function [26-30]. Using our human FXS model, we
335 uncovered a disease-associated increase in overall levels of m^6A modifications and validated
336 these findings in *Fmr1* knockout mice. Our mechanistic studies revealed that the increase in
337 m^6A modifications is the result of translational upregulation of m^6A writers—including key
338 components of the METTL3/14 complex, such as METTL3, METTL14, and WTAP—due to
339 FMRP deficiency. These findings provide new insights into how FMRP deficiency contributes to
340 FXS pathology. However, the selective impact of upregulated m^6A writers on synapse-related

genes in FXS requires further investigation. Additionally, whether and how FMRP deficiency directly regulates the expression of m^6A erasers and readers awaits future mechanistic studies.

To profile transcriptome-wide m^6A modifications, we conducted MeRIP-Seq on neurons derived from FXS patients and postmortem cortical tissues, comparing them with control samples. We identified several synapse-related genes with hypermethylation sites in both FXS neurons and postmortem tissues, suggesting that m^6A dysregulation contributes to FXS-associated synaptic pathology. Notably, expression of many hypermethylated synapse-related genes was also downregulated, and accompanied by increased mRNA decay, indicating that m^6A-mediated gene regulation involves modulating mRNA stability. In mice, m^6A modifications enhances mRNA decay in neural progenitor cells to regulate normal neurodevelopment. Deficiency in m^6A leads to premature differentiation and neurodevelopmental defects[28]. Additionally, studies in *Fmr1* knockout mice revealed that FMRP's antagonistic interaction with the m^6A reader YTHDF2 affects the stability of m^6A-marked target mRNAs [47]. Further mechanistic studies are needed to determine whether YTHDF2 reads m^6A tags on synapse-related transcripts, accelerating their decay in FXS, and whether other m^6A readers (e.g., YTHDF1, YTHDF3, YTHDC1, YTHDC2) modulate other mRNA functions such as alternative splicing and translational efficiency, contributing to FXS pathology.

In conclusion, our patient-derived iPSC model of FXS mimics clinically relevant cortical hyperexcitability and hyperconnectivity phenotypes. As such, our model bridges the gap between experimental models and human disease and holds paramount importance in advancing FXS research. Specifically, we uncovered a novel m^6A-mediated epi-transcriptomic mechanism underlying FXS, where FMRP deficiency leads to increased translation of m^6A writers, resulting in transcriptome-wide hypermethylation. This hypermethylation, in turn, disrupts the stability of synapse-related transcripts, contributing to FXS pathology. Notably, the m^6A writer inhibitor, capable of reducing excessive m^6A modifications, can retore normal mRNA decay and mitigate disease-related synaptic and neuronal defects in FXS iPSCs-derived neurons. Given the challenges in restoring FMRP function in FXS [36,61] and the notable genetic implications of the m^6A reader in ASD [32-35], our findings highlight the translational potential of m^6A modifying drug as novel therapeutic treatment for FXS and ASD. In such future directions, we envision that our FXS patient-derived iPSC model could prove useful in discovery or preclinical candidate validation stages of therapeutic development and thereby improve success rates in later-stage clinical trials.

375 **Limitations of the study**

376 Several limitations remain unresolved and restrict the broader implications of our study. First,
377 human pluripotent stem cell-derived cortical circuitry models do not fully replicate higher-order
378 brain functions, such as cortical oscillations, due to the absence of complex brain structures and
379 connections. This limitation prevents *in vitro* human models from fully capturing patients' clinical
380 phenotypes. Advanced models like human brain assembloids (e.g., cortico-striatum or cortico-
381 thalamus assembloids) and human-mouse chimeric models (where human cortical organoids
382 are engrafted into the cortex of immunodeficient mice) could enhance tissue organization and
383 brain circuitry connectivity, potentially improving the modeling of higher-level brain dysfunction.
384 Additionally, m^6A modifications are highly dynamic and cell-specific during neurodevelopment.
385 Single-cell m^6A sequencing could enable us to track these cell-specific m^6A modifications
386 throughout neurodevelopment, offering deeper insights into their regulatory roles in both normal
387 cortical development and FXS pathogenesis. Lastly, only male subjects were examined in this
388 study. Future comparisons between female and male FXS subjects could uncover sex-specific
389 differences in m6A-mediated epi-transcriptomic dysregulation in FXS.

390 **Methods**

391 **Participants.**

392 Seven participants with a full mutation in the *FMR1* gene were recruited through the Cincinnati
393 Fragile X Research and Treatment Center (Supplemental Table 1). Fragile X status was
394 confirmed by southern blotting and PCR analysis completed at Rush University. Five typically
395 developing control (TDC) were recruited through web-based fliers from the local community and
396 had no prior diagnosis or treatment for developmental or neuropsychiatric disorders. Written
397 informed consent was obtained from all participants or their legal guardians, with verbal assent
398 provided when appropriate. This study was approved by the Institutional Review Board (IRB) of
399 Cincinnati Children's Hospital Medical Center (CCHMC) and was conducted in accordance with
400 all relevant guidelines and regulations, including the Declaration of Helsinki.

401 Deviation intelligence quotient (IQ) scores, including full-scale IQ (FSIQ), non-verbal IQ
402 (NVIQ), and verbal IQ (VIQ), were assessed using the Stanford-Binet Intelligence Scales, 5th
403 Edition, with adjustments made to account for floor effects commonly seen in individuals with
404 developmental disabilities [62].

405 Blood samples were collected from seven FXS and one TDC participants for various
406 analyses: one set was used for peripheral blood mononuclear cells (PBMCs) isolation and FXS
407 induced pluripotent stem cells (iPSCs) generation, another for FMRP quantification using an
408 optimized Luminex assay as described by Boggs *et al.* [63], and a third for *FMR1* mRNA detection
409 via a sensitive RT-qPCR assay as previously described [64].

410

411 **Human postmortem brain tissue.**

412 Frozen human postmortem brain tissues (Brodmann area 44; Supplemental Table 2), including
413 samples from three FXS patients [named human FXS (hFXS)-1, hFXS-2, and hFXS-3] and
414 three age-matched control subjects [named human unaffected healthy control (hUHC) -1,
415 hUHC-2, and hUHC-3], were obtained from the National Institutes of Health (NIH)
416 Neurobiobank, specifically the University of Maryland Brain and Tissue bank, and the Brain
417 Tissue Donation Program at the University of Pittsburgh.

418

419 **Generation and culture of patient iPSC lines.**

420 Whole blood samples were collected from seven male FXS and one TDC participate. PBMCs
421 were isolated using SepMate™-50 tubes (StemCell Technologies) with Lymphoprep™ Density
422 Gradient Medium (StemCell Technologies) through density-gradient centrifugation. A total of
423 500,000 PBMCs were seeded in 24-well plates and cultured in PBMC medium [StemPro®-34

424 SFM medium (ThermoFisher) supplemented with SCF (100ng/mL; Peprotech), FLT-3
425 (100ng/mL; Peprotech), IL-3 (20ng/mL; Peprotech), and IL-6 (20ng/mL; Peprotech)] for
426 four days. PBMCs were then transduced using the Cytotune™-iPS 2.0 Sendai Reprogramming
427 Kit (ThermoFisher) at the appropriate MOI, following the manufacturer's instructions, and
428 incubated overnight. The next day, the CytoTune™ 2.0 Sendai viruses were removed, and the
429 transduced PBMCs were cultured in PBMC medium for two additional days. The cells were
430 subsequently seeded on vitronectin (ThermoFisher)-coated plates in complete StemPro®-34
431 SFM medium without cytokines for four days. After this, the medium was switched to Essential
432 8™ Flex medium (ThermoFisher). Once iPSC-like colonies emerged, they were manually
433 picked and cultured in Essential 8™ Flex medium. These FXS iPSCs were labeled FXS-1, FXS-
434 2, FXS-3, FXS-4, FXS-5, FXS-6, FXS-7, separately. The TDC control iPSC was labeled UHC-5.
435 UHC fibroblast samples derived from five age-matched male subjects were obtained from the
436 Coriell Institute (GM00409, GM07753, GM09503, GM23815, GM23976). These fibroblasts were
437 reprogrammed into iPSCs as previously described in our earlier publication [65]. Briefly, fibroblasts
438 were transduced overnight with Cytotune™-iPS 2.0 Sendai reprogramming vectors, with the
439 medium being changed daily. After seven days, the cells were transferred into vitronectin-coated
440 plates with Essential 8™ Flex medium. iPSC colonies were identified, manually picked, and
441 expanded approximately 18 days later. These control iPSCs were named UHC-1, UHC-2, UHC-
442 3, UHC-4, UHC-6, separately. Another control iPSC line, C3, previously published[66] and
443 generously provided by Dr. Hongjun Song and Guo-li Ming's labs, was renamed UHC-7 for this
444 study.
445 All iPSCs were expanded on vitronectin-coated plates in Essential 8™ Flex medium and
446 passaged with ReleSR™ (StemCell Technologies) upon reaching 70-80% confluence using a
447 1:6 split ratio. iPSCs were cryopreserved in stem cell freezing medium [American Type Culture
448 Collection (ATCC)]. 10 μM Y27632 (Peprotech) was added during both passaging and thawing.
449 All iPSCs generated in this project have been carefully characterized in terms of their karyotype,
450 pluripotency, and expression of stemness markers.
451
452 **CGG sizing.**
453 Genomic DNA was extracted from iPSCs using the Quick-DNA Miniprep Kit (Zymo Research).
454 The CGG repeat size in the *FMR1* gene was determined by repeat-primed PCR (RP-PCR)
455 using primers flanking the CGG-repeat region of the 5' UTR in *FMR1*, as per the manufacturer's
456 instructions (AmplideX ® PCR/CE *FMR1* Kit, Asuragen). Briefly, 2 μl of purified genomic DNA
457 (40 ng/μl) was added to a master mix containing 11.45 μl GC-Rich Amp Buffer, 0.5 μl *FMR1* F, R

458 FAM-Primers, 0.5 µl *FMR1* CGG Primer, 0.5 µl diluent, and 0.05 µl GC-Rich Polymerase Mix.
459 The PCR protocol included: initial denaturation at 95 °C for 5 min, followed by 10 cycles of 97
460 °C for 35 s, 62 °C for 35 s, and 68 °C for 4 min. This was followed by 20 cycles of 97°C for 35
461 seconds, 62°C for 35 seconds, and 68°C for 4 minutes, with an additional 20-second increment
462 per cycle. The final extension was carried out at 72°C for 10 minutes. The PCR products were
463 then mixed with Hi-Di Formamide and the ROX 1000 Size Ladder. After denaturation at 95 °C
464 for 2 min and cooling to 4°C for 5 minutes, the amplicons were separated via capillary
465 electrophoresis (CE) using an ABI 3500 Genetic Analyzer with POP-7 polymer (Applied
466 Biosystems). The CGG repeat length was calculated based on the fragment size in base pairs
467 using the *FMR1* Analysis Macro (v2.1.2; Asuragen) with size and mobility conversion factors.
468
469 **Differentiation of cortical glutamatergic neurons from iPSCs**
470 Cortical glutamatergic neurons were generated from iPSCs as previously described[67,68], with
471 some modifications as described here. Briefly, iPSCs were dissociated into single cells with
472 StemPro™ Accutase™ Cell Dissociation Reagent (ThermoFisher) and seeded at a density of
473 2,500,000 cells per well on Matrigel-coated (human embryonic stem cell-qualified matrix,
474 Corning) six-well plates in Essential 8™ Flex medium with Y27632. From day 1 to day 3, the
475 medium was switched to Essential 6™ medium (ThermoFisher) supplemented with LDN193189
476 (500 nM, Peprotech), SB431542 (10 µM, Cayman Chemical), and XAV939 (5 µM, Selleckchem)
477 (referred to as E6-LSBX medium). From day 4 to day 8, cells were maintained in E6-LSB
478 medium (without XAV939). Beginning on day 9, the medium was switched to a house-made N2
479 medium [DMEM/F12 medium with 2-mercaptoethanol (1X; ThermoFisher), sodium bicarbonate
480 (2 mg/mL; Sigma), D-(+)-Glucose (1.56 mg/mL; Sigma), progesterone (6.4 mg/mL; Sigma), N2
481 Supplement-B (0.5X; StemCell Technologies)], supplemented with B27™ (1X; ThermoFisher)
482 and FGF-8b (50ng/mL; R&D Systems) until day 21. At this stage, neuronal progenitor cells
483 (NPCs) were either cryopreserved in stem cell freezing medium or dissociated with Accutase™
484 and plated onto Poly-L-ornithine (PO, 15 µg/mL; Sigma)/Laminin (2 µg/mL; R&D
485 Systems)/Fibronectin (1 µg/mL; R&D Systems)-coated plates or coverslips. Cells were then
486 cultured in neuron medium [Neurobasal® medium (ThermoFisher) with B27™ supplement (1X),
487 BDNF (20 ng/mL; Peprotech), GDNF (20 ng/mL; Peprotech), Ascorbic Acid (AA, 0.2 mM;
488 Sigma), cAMP (100 µM; Sigma), GlutaMAX™ (1X; ThermoFisher), and MEM Non-Essential
489 Amino Acids (NEAA, 1X; ThermoFisher)] with the addition of DAPT (10 µM; Cayman Chemical).
490 Half of the neuron medium was replaced twice a week for a total of six weeks.
491

492 **Isolation of primary mouse astrocytes and co-culture with iPSC-derived cortical neurons.**
493 Primary mouse astrocytes were isolated as previously described [69], with minor modifications.
494 Brains from P0 C57BL/6J mice were dissected, and the meninges were removed. The
495 meninges-free cerebral cortices were minced into small pieces and digested with trypsin
496 (ThermoFisher) and DNase I (Sigma). The resulting cell suspension was plated onto 0.01%
497 Poly-L-Lysine (PLL; Sigma)-coated flasks in Dulbecco's Modified Eagle Medium (DMEM,
498 ThermoFisher) supplemented with 10% fetal bovine serum (FBS) (ThermoFisher). and 2%
499 penicillin/streptomycin. From day 2 to day 8, primary astrocytes were separated from
500 oligodendrocyte progenitor cells, microglia and neurons by tapping the flask and washing with
501 PBS. Primary astrocytes were cryopreserved around day 8.
502 Before co-culturing with cryopreserved iPSC-derived NPCs, primary mouse astrocytes
503 were thawed, expanded and seeded on coverslips in 24-well plates. Once the astrocyte
504 monolayer reached 80-90% confluence, cryopreserved iPSC-derived NPCs were thawed,
505 seeded directly onto the astrocytes, and differentiated in neuron medium [Neurobasal® medium
506 supplemented with B27™, BDNF, GDNF, AA, cAMP, GlutaMAX™, and NEAA] containing DAPT.
507 Half of the neuron medium was replaced twice weekly. After 6 weeks of culture, whole-cell patch
508 clamp recordings and immunocytochemistry were performed. For treatment, cultures were
509 exposed to either DMSO (0.1%; Sigma) or 10 μM STM2457 (Cayman Chemical) for 2 weeks,
510 from week 4 to week 6.
511
512 **Western blot analysis.**
513 Ten-week-old wild-type (WT) and *Fmr1*-knockout (*Fmr1*-KO) male mice, kindly provided by Prof.
514 Christina Gross, were used for protein extraction from fresh cortical tissues. Additionally, protein
515 was extracted from six-week-old iPSC-derived cortical neurons using ice-cold RIPA buffer
516 (Sigma), supplemented with cOmplete Protease Inhibitor Cocktail (Roche) and PhosSTOP™
517 (Roche). Lysates were sonicated and incubated on ice, followed by centrifugation at 4°C.
518 Protein concentrations were determined using the Pierce™ BCA Protein Assay Kit
519 (ThermoFisher). Equal amounts of protein lysates were denatured in SDS-polyacrylamide gel
520 electrophoresis (PAGE) Sample Loading Buffer (G-Biosciences), separated on 4-12% Bolt Bis-
521 Tris Plus Protein Gels (ThermoFisher), and transferred to polyvinylidene fluoride (PVDF)
522 membranes (Millipore) using the XCell SureLock™ Mini-Cell system (ThermoFisher). The
523 membranes were blocked for 1 hour at room temperature (RT) with 5% non-fat milk in Tris-
524 buffered saline containing Tween-20 (TBST) (blocking buffer), followed by overnight incubation
525 at 4°C with the following primary antibodies diluted in blocking buffer: rabbit polyclonal anti-

526 FMRP (1:1000; Abcam), rabbit monoclonal Synapsin II (1:1000; Abcam), mouse monoclonal
527 SV2 (1:1000; DSHB), rabbit monoclonal METTL3 (1:500; MedChemExpress), rabbit polyclonal
528 METTL14 (1:1000; Sigma), rabbit monoclonal WTAP (1:500; Cell Signaling Technology), and
529 mouse monoclonal GAPDH (1:5000; Santa Cruz Biotechnology). After 3 washes with TBST, the
530 membranes were incubated for 1 hour at RT with horseradish peroxidase (HRP)-coupled
531 secondary antibodies: anti-rabbit IgG (1:5000; ThermoFisher) or anti-mouse IgG (1:5000;
532 ThermoFisher). The membranes were washed 3 times with TBST and visualized by the addition
533 of SuperSignal™ West Pico PLUS Chemiluminescent Substrate (ThermoFisher) directly on the
534 membranes placed in the iBright™ FL 1500 Imaging System (ThermoFisher). Protein levels were
535 normalized to GAPDH, and quantitative analysis was performed using ImageJ software.
536
537 **Immunocytochemistry.**
538 Six-week-old iPSC-derived cortical neurons were fixed with 4% paraformaldehyde
539 (ThermoFisher) for 15 min at RT, then washed 3 times with PBS. They were permeabilized with
540 0.1% Triton™ X-100 (Sigma) and blocked in 3% donkey serum (Sigma) for 2 hours. Primary
541 antibodies, diluted in PBS containing 0.1% Triton X-100 and 3% donkey serum, were applied to
542 the cells and incubated overnight at 4°C. Following primary antibody incubation, cells were
543 treated with species-specific secondary antibodies (1:1000; Jackson ImmunoResearch
544 Laboratories) diluted in 3% donkey serum for 2 hours at RT. Cells were washed and cell nuclei
545 were stained with 4′,6-diamidino-2-phenylindole (DAPI) for 5 min. Coverslips were mounted in
546 fluoroshield mounting medium (Abcam), sealed with clear nail polish, and stored at 2-8°C until
547 imaging. The following primary antibodies were used: mouse monoclonal Nestin (1:500, Santa
548 Cruz Biotechnology), mouse monoclonal Sox2 (1:1000; Santa Cruz Biotechnology), mouse
549 monoclonal ZO1 (1:1000; Thermo Fisher Scientific), rabbit polyclonal Foxg1 (1:1000, Abcam),
550 mouse monoclonal PAX6 (1:1000; BD Biosciences), mouse monoclonal OTX2 (1:50; DSHB),
551 rabbit polyclonal doublecortin (1:1000; Cell Signaling Technology), mouse monoclonal BRN2
552 (1:50; DSHB), goat monoclonal CaMKII (1:500; Santa Cruz Biotechnology), mouse polyclonal
553 beta III tubulin (1:500; Sigma), rabbit polyclonal TBR1 (1:1000; Abcam), rat monoclonal CTIP2
554 (1:1000; Abcam), rabbit monoclonal Synapsin I (1:1000; Millipore), mouse monoclonal SV2
555 (1:1000; Santa Cruz Biotechnology).
556 Images were obtained on either a Nikon A1R inverted confocal laser scanning
557 microscope with 60x objectives or an Olympus BX51 with 20x objectives. Image analysis was
558 performed using NIS Elements version 5.42.06 software (Nikon) and Imaris version 10.2.0
559 software (Nikon). For neurite analysis, parameters including the number of segments, total

560 length, terminal points, branch points, maximum segment length, minimum segment length, and
561 mean segment length were assessed. Synaptic density (D) was determined by calculating the
562 total SV2 and SYN1 puncta per 100 μm of total dendritic length. For spine analysis, the ratio of
563 mature (stubby and mushroom-like) and immature spines (filopodia and thin-like) was
564 calculated.
565
566 **Whole-cell patch clamp recording.**
567 Whole-cell patch-clamp recordings were conducted at RT on iPSC-derived cortical neurons,
568 either untreated or treated with DMSO or STM2457 for 2 weeks, following a six-week co-culture
569 with primary mouse astrocytes, using a Multiclamp 700A patch-clamp amplifier (Molecular
570 Devices) as previously described [34]. Briefly, cortical neurons grown on coverslips were
571 visualized with a 40X air objective on an inverted Zeiss microscope, and the recording chamber
572 was constantly perfused with a bath solution consisting of 128 mM NaCl, 30 mM glucose, 25
573 mM HEPES, 5 mM KCl, 2 mM $CaCl_2$, and 1 mM $MgCl_2$ (pH 7.3; 315–325 Osm). Patch pipettes
574 were pulled from borosilicate glass (Sutter Instrument) with a resistance of 3-5 MΩ and filled
575 with an internal solution composed of 135 mM CsGluconate, 10 mM Trisphosphocreatine, 10
576 mM HEPES, 2.5 mM EGTA, 4 mM MgATP, 0.5 mM Na_2GTP, and 5 mM QX-314 (pH 7.3 with
577 CsOH; ~305 mOsm) for excitatory postsynaptic currents (EPSCs) and inhibitory postsynaptic
578 currents (IPSCs). EPSCs were recorded at a holding potential of -70 mV, while IPSCs were
579 recorded at +20 mV. The series resistance was typically between 10-30 MΩ. To isolate
580 spontaneous IPSCs, the bath solution was supplemented with 10 μM NBQX (Tocris Bioscience)
581 and 50 μM D-AP5 (Tocris Bioscience). For spontaneous EPSC recordings, 20 μM bicuculline
582 (Tocris Bioscience) was added. Drug application was achieved via a gravity-driven drug delivery
583 system (VC-6, Warner Instruments). Spontaneous IPSCs and EPSCs were recorded for 4
584 minutes (starting 2 minutes after break-in, to allow QX-314 to block sodium currents) at a
585 holding potential, sampled at 10 kHz, and filtered at 1 kHz. Spontaneous and evoked action
586 potentials were recorded using current clamp, while sodium and potassium currents were
587 measured using voltage clamp. Data acquisition was performed using pClamp 9 software
588 (Molecular Devices), and spontaneous synaptic events were analyzed with MiniAnalysis
589 software (Synaptosoft).
590
591 **Microelectrode array (MEA) and analysis.**
592 The 64-channel multielectrode array (MEA) recording system (MED64, Alpha MED Scientific)
593 features an array of 64 planar microelectrodes arranged in an 8 × 8 pattern (50 × 50 μm

594 electrodes with 150 μm spacing) and was used to non-invasively monitor the electrical activity of
595 neuronal networks. Before use, the surface of the MED64 probe was coated with
596 PO/laminin/fibronectin and a drop of iPSC-derived NPCs (500,000 cells) were directly plated on
597 the top of the electrodes and cultured in B-27™ Electrophysiology Kit supplemented with BDNF
598 (20 ng/ml), GDNF (20 ng/ml), AA (0.2 mM), cAMP (100 μM), GlutaMAX (1X), and NEAA (1X).
599 DAPT was administered on day 1 to synchronize neuronal maturation, and the cultures were fed
600 weekly. Spontaneous neuronal activity was recorded from weeks 4 to 8 post-differentiation for 5
601 minutes at a sampling rate of 20 kHz using Mobius software (Alpha MED Scientific). Data were
602 filtered with a 1-1000 Hz frequency bandwidth.
603 A spike was detected when the recorded signal exceeded a threshold of ± 5.5 σ, where σ
604 was the standard deviation (SD) of the baseline noise during quiescent periods. Spike clustering
605 was performed using the Mobius software's 'Cluster Spikes' panel to distinguish and separate
606 signals from multiple cells recorded on a single channel based on the shapes of their spikes,
607 utilizing a modified version of the online 'Leader-Follower Clustering' algorithm. A valid cluster
608 was defined by the following parameters: a minimum of 5 spikes ('Min # spikes') and 30%
609 similarity ('Similarity %'). Next, burst activity and synchronized burst activity were analyzed by
610 Mobius offline toolkit software (Alpha Med Scientific). Bursts were identified as sequences of at
611 least three spikes with inter-spike intervals within 300 milliseconds and a duration exceeding
612 200 milliseconds. Burst duration and spikes per burst were analyzed and compared.
613 Synchronized burst activity, representing burst events across 64 channels, was visualized using
614 a 'time course of spike frequencies across 64 channels' plot, where spike frequencies were
615 quantified as the array-wide spike detection rate (ASDR). Additionally, a raster plot was used to
616 display the distribution of spike timing across all channels.
617 Moreover, MEA data were analyzed using UP state analysis, a method previously applied
618 to *in vitro* brain slices from *Fmr1*-KO mice [70]. Spontaneous UP states were detected based on
619 methods defined in Hays et al[70]. For each channel, data were normalized to zero by subtracting
620 average, and rectified. Rectified data were then low pass filtered at 0.2 Hz. UP states were
621 identified when the amplitude of the filtered signal exceeded the root mean square threshold for
622 a minimum of 200 milliseconds. Events within 600 milliseconds of each other were grouped
623 together into a single UP state. Median duration of up states as well as interval between up
624 states was calculated for each channel.
625
626 **EEG recording and preprocessing**

627 Five minutes of resting state EEG data were collected from four FXS and four TDC participants.
628 Their epidemiological information is listed in Supplemental Table 1. To facilitate cooperation in
629 FXS patients, participants watched a silent video during recording. EEG data were recorded
630 with a 128-electrode saline-based Hydrocel system (Magstim/EGI) at a sampling rate of 1000
631 Hz.
632 EEG data were blinded, and all preprocessing was performed using EEGLAB (EEGLAB)[71].
633 The data were filtered offline using a bandpass filter from 0.5 to 120 Hz, and a notch filter at 60
634 Hz was used to remove power line noise. EEG data was visually inspected for channels or
635 periods affected by excessive artifacts from muscle, movement, and channel noise. Removed
636 channels were interpolated using spherical spline interpolation. Independent component
637 analysis (ICA) decomposition was performed using the EEGLAB pop_runica function, and
638 components were visually inspected to identify and remove those containing muscle, channel,
639 and eye movements. The data were then referenced to average.
640
641 **EEG Analysis**
642 Preprocessed EEG data were analyzed using MNE (v1.6.1) and the FOOOF toolbox (v1.1.0).
643 Power spectral density (PSD) was calculated at each electrode using Welch's method, with two
644 second segments and 50% overlap. For each subject, the PSD was averaged across all
645 channels excluding two outer rows of peripheral channels, to minimize the effect of remaining
646 muscle and movement artifact. The FOOOF toolbox was used to model the periodic and
647 aperiodic components of the average PSD for each subject. The model was computed using the
648 fixed aperiodic mode, with peak width limits of 1 to 12 Hz, maximum peak number set to 6, peak
649 threshold of 2 standard deviations, and no minimum peak height.
650
651
652 **m^6A dot blot assay on cortical neurons and *Fmr1*-KO mouse brain tissue.**
653 Ten-week-old WT and *Fmr1*-KO male mice were used for RNA extraction from fresh cortical
654 tissues. Additionally, total RNA was extracted from six-week-old iPSC-derived cortical neurons
655 using TRIzol reagent (ThermoFisher), followed by purification with Dynabeads mRNA
656 Purification Kit (ThermoFisher) according to the manufacturer's instructions. The extracted
657 mRNA was denatured and spotted onto Hybond N+ membrane (GE Healthcare), then cross-
658 linked using a Stratalinker UV Crosslinker 2400 (Stratagene). The membrane was blocked with
659 5% milk in PBST and probed overnight at 4°C with a rabbit m^6A antibody (1:250; Synaptic
660 Systems), followed by incubation with HRP-conjugated anti-rabbit IgG secondary antibody

661 (1:5000). Detection was carried out using SuperSignal™ West Pico PLUS Chemiluminescent
662 Substrate, and images were captured using the iBright™ FL 1500 Imaging System. To
663 determine the total RNA input, the membrane was stained with 0.04% methylene blue (Sigma)
664 in 0.5M sodium acetate (Millipore) prior to blocking. Quantification of dot intensity was
665 performed using ImageJ software.
666
667 **RIP-RT-qPCR.**
668 HEK293T cells were grown in DMEM supplemented with 10% FBS and transfected using
669 Lipofectamine 3000 (Thermo Fisher Scientific) according to the manufacturer's protocol. Cells
670 were either co-transfected with *FMRP-Flag* and *FUGW* plasmids or transfected with *mCherry-*
671 *Flag* plasmids. Post-transfection, cells were lysed using 1 mL of RIP lysis buffer (10 mM HEPES
672 pH 7.4, 200 mM NaCl, 30 mM EDTA, 0.5% Triton X-100) supplemented with protease inhibitors
673 and SUPERaseIN (1:500; ThermoFisher) at 4°C with rotation for 30 minutes. Cell lysates were
674 then cleared by centrifugation at 20,000× g at 4°C for 15 min. 10% of the supernatant was
675 saved for RNA extraction and protein extraction as input controls. The remaining supernatants
676 were incubated overnight at 4°C with ANTI-FLAG® M2 Affinity Gel (Sigma) with rotation. The
677 immunoprecipitated protein-RNA complexes were subsequently washed three times with RIP
678 wash buffer (10 mM HEPES, pH 7.4, 400 mM NaCl, 30 mM EDTA, 0.5% Triton X-100, 2X
679 protease inhibitors, and 1:1000 SUPERaseIN). Saved input and immunoprecipitated proteins
680 were eluted with sample loading buffer for SDS-PAGE, followed by western blotting using rabbit
681 polyclonal FMRP (1:1000; Abcam) and mouse monoclonal GAPDH (1:5000; Santa Cruz
682 Biotechnology). The saved input and immunoprecipitated RNA were extracted with TRIzol
683 reagent (ThermoFisher) and subjected to RT-qPCR with primers (listed in Table S1), normalizing
684 to input RNA. Reverse transcription was performed using the High-Capacity cDNA Reverse
685 Transcription Kit (ThermoFisher), and RT-qPCR was conducted using PowerUp SYBR Master
686 Mix (ThermoFisher) on a QuantStudio system.
687
688 **Polysome profiling and polysome-associated mRNA analysis.**
689 Sucrose density gradient centrifugation was employed to separate the ribosome fractions as
690 described previously [59]. Briefly, six-week-old cortical neurons were cultured with 100 µg/mL
691 cycloheximide (CHX; Sigma) supplement for 10 min at 37 °C prior to cell harvest. Cells were
692 washed in ice-cold PBS containing 100 µg/mL CHX and harvested in polysome lysis buffer (5
693 mM Tris-HCl, pH7.5, 2.5 mM MgCl2, 1.5 mM KCl, 1 mM DTT,0.5% Triton X-100, 0.5% sodium
694 deoxycholate, 100 µg/mL CHX, 40 U/ml RNaseOUT, 0.2 mg/mL heparin and protease inhibitor

695 cocktail). Cells were lysed by pipetting several times and incubation on ice for 15 min, followed
696 by centrifugation at 10,000 x g for 10 min at 4 °C. 10–50% linear sucrose gradient was
697 prepared using Biocomp Gradient Master 108 with pre-layered 10% and 50% sucrose in the
698 gradient buffer (5 mM Tris-HCl, pH7.5, 2.5 mM MgCl2,1.5 mM KCl, 2 mM DTT, 100 µg/mL CHX,
699 40 U/ml RNaseOUT, 0.1 mg/mL heparin and protease inhibitor cocktail). 300 µl supernatant of
700 cell lysate was layered on the top the sucrose gradient and centrifuged at Beckman SW41 rotor
701 in Beckman Ultra-clear tube at 4 °C, 39K rpm for 2 hrs. Gradients were fractionated while
702 monitoring absorbance at A260 with a Biocomp Piston Gradient Fractionator system according
703 to the manufacturer protocol. The areas of monosome fractions (#6-11) and heavy polysome
704 fractions (#18-25) were calculated using GraphPad Prism 6 (GraphPad Software Inc.). Total
705 RNA in each fraction was isolated using TRIzol Reagent. 200 ng of RNA in each fraction was
706 reverse transcribed to cDNA using a High-Capacity cDNA Reverse Transcription Kit. RT-qPCR
707 for target genes (*WTAP*, *METTL3* and *METTL14*) in each fraction were carried out using
708 PowerUp SYBR Master Mix. The target gene mRNA in each fraction was normalized to *GAPDH*
709 in this fraction; the abundance in the heavy polysomes was calculated by summing up fractions
710 #18-25 and compared between UHC and FXS cortical neurons.
711
712 **MeRIP-seq, MeRIP-RT-qPCR and analysis**
713 The mRNAs from total RNAs were isolated from six-week-old cortical neurons, as well as
714 postmortem brain tissues, using Dynabeads mRNA Purification Kit. Purified mRNA samples
715 were fragmented to 100-200 nt with 10X RNA Fragmentation Buffer (100 mM Tris-HCl, 100 mM
716 $ZnCl_2$ in nuclease-free H_2O). The reaction was stopped by adding 10X EDTA (0.5M). 10% of the
717 fragmented RNA was set aside as an input sample, while the remaining RNA was used for m^6A
718 immunoprecipitation. The fragmented RNA was incubated with anti-m^6A antibody (Synaptic
719 Systems) for 3 h at 4°C and then with protein G magnetic beads (ThermoFisher) at 4°C for an
720 additional 2 h to obtain immunoprecipitated RNA fragments. The m^6A-enriched RNA was
721 extracted using TRIzol. The library was prepared following the instructions for Kapa RNA
722 HyperPrep Kit (Roche). Both the input samples without IP and the m^6A IP samples were
723 subjected to 150-bp, paired-end sequencing on an Illumina NovaSeq 6000 sequencer at CD
724 Genomics.
725 For MeRIP-seq analysis, quality control of raw sequencing reads was assessed using
726 FastQC (v0.11.7). Raw reads in fastq format were then subjected to trimming, eliminating
727 adaptor sequences, reads with adaptor contaminants, and low-quality reads, using Trim Galore
728 (v0.6.6). The preprocessed reads were aligned to the human genome (GRCh38) employing

729 STAR (v2.7.9) with default settings. m^6A peaks were identified using the R package exomePeak
730 (v2.16.0) with the following parameters: “PEAK_CUTOFF_PVALUE = NA,
731 PEAK_CUTOFF_FDR = 0.05, FRAGMENT_LENGTH = 200”. The distributions of m^6A peaks
732 across the chromosomes in both UHC and FXS cortical neurons were analyzed using circos
733 (v0.69.8). Differential m^6A peak were identified using exomePeak R package under parameters:
734 “PEAK_CUTOFF_PVALUE = NA, PEAK_CUTOFF_FDR = 0.05, FRAGMENT_LENGTH=200”.
735 The output “sig_diff_peak” file was further filtered using the condition “diff.lg.fdr > 2”, generating
736 a highly significant differential m^6A peak file between FXS and control neurons (Table S2), as
737 well as between hFXS and hUHC postmortem brain tissues (Table S4). This dataset was then
738 categorized into hypermethylated and hypomethylated m^6A peaks based on the diff.log2.fc
739 values. Peaks with “diff.log2.fc” > 0 were classified as hypermethylated, while those with
740 “diff.log2.fc” < 0 were classified as hypomethylated (Table S2 and S4). Identified m^6A peaks
741 were visualized using the Integrative Genomics Viewer (IGV, v2.15.4) with bam formats. Gene
742 ontology (GO) analysis was performed using the clusterProfiler R package (v4.11.0), with
743 visualizations generated in RStudio (v3.4.3) using the ggplot2 package (v3.5.1). In the plots,
744 circle size corresponds to the percentage of genes in each ontology group, and color represents
745 the p-value for gene enrichment associated with each GO term. m^6A-RNA-related genomic
746 features were visualized using Guitar R package (v2.14.0), and de novo motif analysis was
747 performed with homer (v4.11).
748 To examine m^6A modifications on individual genes in six-week-old cortical neurons,
749 MeRIP-RT-qPCR was performed using the same procedures, except that RNAs were sheared
750 into approximately 200 nt fragments. Total RNAs were isolated from neurons untreated or
751 treated with DMSO or STM2457 for 48 hours. Primers were designed to target different m^6A
752 modification sites identified through MeRIP-seq data, including 5 sites for *APC2*, 1 site for
753 *CASKIN1,* 2 sites for *LRRC4B,* 2 sites for *NRXN2,* 1 site for *SLC8A2,* and 1 site for *SYP.* All
754 primers used for MeRIP-RT-qPCR are listed in Table S1. RT-qPCR was conducted using
755 PowerUp SYBR Master Mix on a QuantStudio system. m^6A enrichment was determined by RT-
756 qPCR analysis, calculating the percentage of a target gene in IP fraction relative to the input
757 fraction using the formula: %Input = $2^{\wedge}$ (Ct of target gene in IP - adjusted Ct of target gene in
758 input).
759
760 **Bulk RNA sequencing and analysis.**
761 Total RNAs were extracted from six-week-old cortical neurons using TRIzol reagent followed by
762 mRNAs isolation with the Dynabeads mRNA Purification Kit. Sequencing libraries were

763 prepared using NEBNext Ultra RNA Library Prep kit (New England Biolabs) for Illumina
764 following manufacturer's protocol. Briefly, mRNAs were fragmented and reverse-transcribed to
765 synthesize double-stranded cDNAs. After end repair and 3' adenylation, Illumina-compatible
766 adapters for multiplexing were ligated to the ends of the double-stranded cDNA fragments. The
767 ligation products were then amplified and purified to generate sequencing libraries. Sequencing
768 was performed on an Illumina NovaSeq 6000 platform with 150 bp paired end reads at
769 Novogene Bioinformatics Technology Co., Ltd (Beijing, China).
770 For RNA-seq analysis, similar to the MeRIP-seq workflow, sequence reads obtained from
771 RNA-seq were initially processed and aligned to the human genome (GRCh38) employing
772 STARwith default settings. Gene counts were obtained using FeatureCounts (v2.0.3).
773 Differential expression analysis was performed using the R package DESeq2 (v1.42.1), with a p
774 value cutoff of 0.05 and a fold change threshold of log2 (fold change) > ±1. The differentially
775 expressed genes (DEGs) between FXS and UHC cortical neurons were presented in Table S3.
776 GO enrichment analysis was performed using the clusterProfiler R packagefor functional
777 annotation.
778 DEGs between hFXS and hUHC postmortem brain tissues were identified using the
779 MeRIP-seq input sequencing data, following the aforementioned RNA-seq data analysis
780 pipeline. These DEGs are presented in Table S5. Additionally, published MeRIP-seq data for two
781 *Fmr1*-KO and two WT mice (GSE107434) were downloaded from the NCBI Gene Expression
782 Omnibus (GEO) database (https://www.ncbi.nlm.nih.gov/geo/query/acc.cgi?acc=GSE107434)
783 and re-analyzed using the MeRIP-seq input sequencing data, following the aforementioned
784 RNA-seq analysis pipeline for DEGs. The DEGs between *Fmr1*-KO and WT mice brain cortex
785 tissues are presented in Table S6.
786
787 **RNA stability assay**
788 For six-week-old cortical neurons, treated or untreated with DMSO or STM2457 for 48 hours,
789 transcription was inhibited by adding 5 μg/ml of actinomycin D (Cayman Chemical). Cells were
790 harvested at 0-, 2-, and 6-hours post-actinomycin D treatment, washed with PBS, and lysed in
791 TRIzol. Reverse transcription was performed using the High-Capacity cDNA Reverse
792 Transcription Kit. RT-qPCR for target genes (*SYT7*, *LRRC4B*) was then conducted using
793 PowerUp SYBR Master Mix on a QuantStudio system. Gene expression levels were normalized
794 to *GAPDH*. All primers used are listed in Table S1.
795
796 **Data collection and statistics.**

All experiments were performed in triplicate or more, with data collected from parallel cultures. Detailed sample sizes and descriptions of the sample collection are provided in each figure legend. Quantitative data are presented as mean ± S.E.M. The specific statistical tests used for comparisons are indicated in the corresponding figure legends. A significance threshold of $p < 0.05$ was applied. Statistical analyses, including two-tailed t-tests, Chi-square tests, one-way ANOVA with multiple comparisons, and two-way ANOVA with multiple comparisons, were conducted using RStudio (v3.4.3) and GraphPad Prism 6.

Data and code availability.

The RNA-seq data generated in this study has been deposited in the GEO database under accession number GSE278697. The m^6A-seq data has also been submitted to GEO with accession number GSE278698. Additional data, including differential expression genes (DEGs), m^6A peak calling and annotation, FMRP targets, SAFRI ASD genes, synaptic genes, and overlap analyses, are provided in the Supplementary Materials (Tables S2-S6). All other relevant data is available upon request from the corresponding author. Commands used to run software such as STAR, exomePeak, Homer, and Guitar are included in the respective software manuals, which are publicly accessible online. R scripts used for bioinformatics analyses are available upon request.

REAGENT or RESOURCE	SOURCE	IDENTIFIER
Antibodies		
FMRP	Abcam	Cat# ab17722; RRID: AB_2278530
Synapsin II	Abcam	Cat# ab76494; RRID: AB_2200420
SV2	DSHB	SV2; RRID: AB_2315387
METTL3	MedChemExpress	Cat# HY-P80223
METTL14	Sigma	Cat# HPA038002; RRID: AB_10672401
WTAP	Cell Signalling Technology	Cat# 41934; RRID: AB_2923053
GAPDH	Santa Cruz Biotechnology	Cat# sc-32233; RRID: AB_627679
Nestin	Santa Cruz Biotechnology	Cat# sc-23927; RRID: AB_627994
Sox2	Santa Cruz Biotechnology	Cat# sc-365823; RRID: AB_10842165
ZO1	ThermoFisher	Cat# 33-9100; RRID: AB_2533147
Foxg1	Abcam	Cat# ab18259; RRID: AB_732415
PAX6	BD Biosciences	Cat# 561462; RRID: AB_10715442
OTX2	DSHB	Cat# PCRP-OTX2-1F7; RRID: AB_2618925
DCX	Cell Signaling Technology	Cat# 4604; RRID: AB_561007
BRN2	DSHB	Cat# PCRP-POU3F2-1A3; RRID: AB_2618965
CaMKII	Santa Cruz Biotechnology	Cat# sc-5391; RRID: AB_634553
beta III tubulin	Sigma	Cat# T8660; RRID: AB_477590
TBR1	Abcam	Cat# ab31940; RRID: AB_2200219
CTIP2	Abcam	Cat# ab18465; RRID: AB_2064130
Synapsin I	Millipore	Cat# 574777; RRID: AB_2200124
GFP	Aves lab	Cat# GFP-1010; RRID: RRID:AB_2307313

m^6A antibody	Synaptic Systems	Cat# 202 003; RRID: AB_2279214
anti-mouse IgG (H+L) secondary antibody, HRP	ThermoFisher	Cat# 31430; RRID: AB_228307
anti-rabbit IgG (H+L) secondary antibody, HRP	ThermoFisher	Cat# 31460; RRID: AB_228341
Cy2-anti-rabbit IgG (H+L)	Jackson Immuno Research	Cat# 711-225-152; RRID: AB_2340612
Cy2-anti-chicken IgG (H+L)	Jackson Immuno Research	Cat# 703-225-155; RRID: AB_2340370
Cy2-anti-mouse IgG (H+L)	Jackson Immuno Research	Cat# 715-225-150; RRID: AB_2340826
Cy3-anti-rabbit IgG (H+L)	Jackson Immuno Research	Cat# 711-165-152; RRID: AB_2307443
Cy3-anti-mouse IgG (H+L)	Jackson Immuno Research	Cat# 715-165-150; RRID: AB_2340813
Cy5-anti-rat IgG (H+L)	Jackson Immuno Research	Cat# 712-175-150; RRID: AB_2340671
Cy5-anti-goat IgG (H+L)	Jackson Immuno Research	Cat# 705-175-147; RRID: AB_2340415
Cy5-anti-rabbit IgG (H+L)	Jackson Immuno Research	Cat# 711-175-152; RRID: AB_2340607
Bacterial and virus strains		
pFUGW 3flag-mCherry	Lois et al. Christina et al.	Addgene #14883
pscAAV FMRP	This study	
Biological Samples		

Healthy human brain 13164	NIH NeuroBiobank	https://neurobiobank.nih.gov
Healthy human brain 13222	NIH NeuroBiobank	https://neurobiobank.nih.gov
Healthy human brain 13266	NIH NeuroBiobank	https://neurobiobank.nih.gov
FXS human brain 4751	NIH NeuroBiobank	https://neurobiobank.nih.gov
FXS human brain 5006	NIH NeuroBiobank	https://neurobiobank.nih.gov
FXS human brain 5319	NIH NeuroBiobank	https://neurobiobank.nih.gov
Healthy control fibroblast 1	Coriell institute	GM00409
Healthy control fibroblast 2	Coriell institute	GM07753
Healthy control fibroblast 3	Coriell institute	GM09503
Healthy control fibroblast 4	Coriell institute	GM23815
Healthy control fibroblast 5	Coriell institute	GM23976
Chemicals, peptides, and recombinant proteins		
Lymphoprep™ Density Gradient Medium	StemCell Technologies	Cat# 07801
StemPro®-34 SFM Medium	ThermoFisher	Cat# 10639011
SCF	Peprotech	Cat# 300-07
FLT-3	Peprotech	Cat# 300-19
IL-3	Peprotech	Cat# 200-03

IL-6	Peprotech	Cat# 200-06
Vitronectin (VTN-N) Recombinant Human Protein, Truncated	ThermoFisher	Cat# A31804
ReLeSR™	StemCell Technologies	Cat# 100-0484
Y27632	Peprotech	Cat# 1293823
StemPro™ Accutase™ Cell Dissociation Reagent	ThermoFisher	Cat# A1110501
Corning® Matrigel® hESC-Qualified Matrix	Corning	Cat# 354277
Essential 8™ Flex Medium Kit	ThermoFisher	Cat# A2858501
Essential 6™ medium	ThermoFisher	Cat# A1516401
LDN193189	Peprotech	Cat# 1066208
SB431542	Cayman Chemical	Cat# 13031
XAV939	Selleckchem	Cat# S1180
2-Mercaptoethanol	ThermoFisher	Cat# 21985023
Sodium Bicarbonate	Sigma	Cat# S5761
D-(+)- Glucose	Sigma	Cat# G7021
Progesterone	Sigma	Cat# P8783
N2 Supplement-B	StemCell Technologies	Cat# 07156
B-27™ Supplement (50X)	ThermoFisher	Cat# 12587010
Recombinant Human/Mouse FGF-8b Protein	R&D Systems	Cat# 423-F8
Poly-L-ornithine hydrobromide	Sigma	Cat# P3655

Cultrex Mouse Laminin I, Pathclear	R&D Systems	Cat# 3400-010-02
Human Fibronectin Protein, CF	R&D Systems	Cat# 1918-FN-02M
Neurobasal™ Medium	ThermoFisher	Cat# 21103049
Human/Mouse/Rat BDNF Recombinant Protein	Peprotech	Cat# 450-02
Human GDNF Recombinant Protein	Peprotech	Cat# 450-10
L-Ascorbic acid	Sigma	Cat# A5960
N6,2′-O-Dibutyryladenosine 3′,5′-cyclic monophosphate sodium salt (cAMP)	Sigma	Cat# D0627
GlutaMAX™ Supplement	ThermoFisher	Cat# 35050079
MEM Non-Essential Amino Acids Solution (100X)	ThermoFisher	Cat# 11140050
DAPT	Cayman Chemical	Cat# 13197
RIPA Buffer	Sigma	Cat# R0278
cOmplete™ ULTRA Tablets, Mini, *EASYpack* Protease Inhibitor Cocktail	Sigma	Cat# 5892970001
PhosSTOP™	Sigma	Cat# 4906845001
SDS-PAGE Sample Loading Buffer	G-Biosciences	Cat# 786-701

Bolt™ Bis-Tris Plus Mini Protein Gels, 4-12%, 1.0 mm, WedgeWell™ format	ThermoFisher	Cat# NW04125BOX
Bolt™ Transfer Buffer (20X)	ThermoFisher	Cat# BT0006
polyvinylidene fluoride (PVDF) membranes	Millipore	?
TWEEN® 20	Sigma	Cat# P1379
10x Tris Buffered Saline (TBS)	Bio-rad	Cat# 1706435
SuperSignal™ West Pico PLUS Chemiluminescent Substrate	ThermoFisher	Cat# 34580
Stem Cell Freezing Media	ATCC	Cat# ACS-3020-3
Pierce™ 16% Formaldehyde (w/v), Methanol-free	ThermoFisher	Cat# 28908
Triton™ X-100	Sigma	Cat# X100
Donkey serum	Sigma	Cat# D9663
Anti-Fade Fluorescence Mounting Medium - Aqueous, Fluoroshield	Abcam	Cat# ab104135
DNase I	Sigma	Cat# 11284932001
ANTI-FLAG® M2 Affinity Gel	Sigma	Cat# A2220
Dynabeads™ Protein G for Immunoprecipitation 1ml	ThermoFisher	Cat# 10003D

Critical commercial assays		
CytoTune-iPs 2.0 Sendai kit	ThermoFisher	Cat# A16517
Pierce BCA Protein Assay Kit	ThermoFisher	Cat# 23227
Deposited data		
iPSC-derived cortical neurons bulk RNA-seq	This study	GEO: GSE278697
iPSC-derived cortical neurons MeRIP-seq, human brain tissues MeRIP-seq	This study	GEO: GSE278698
Mouse brain tissue MeRIP-seq	Zhang et al.	GEO: GSE107434
Experimental models: Cell lines		
Human: Unaffected healthy control iPSCs 7	Wen et al.	C3
Software and algorithms		
FastQC (v0.11.7)	Babraham Institute	https://www.bioinformatics.babraham.ac.uk/projects/fastqc/
Trim Galore (v0.6.6)	Babraham Institute	https://www.bioinformatics.babraham.ac.uk/projects/trim_galore/
STAR (v2.7.9)	Dobin et al., 2013	https://github.com/alexdobin/STAR
ExomePeak (v2.16.0)	Meng et al., 2013	https://github.com/ZW-xjtlu/exomePeak
Circos (v0.69.8)	Krzywinski et al., 2009	https://circos.ca/; RRID:SCR_011798

Integrative Genomics Viewer (IGV, v2.15.4)	James et al., 2011	http://www.broadinstitute.org/igv/; RRID:SCR_011793
Rstudio (v3.4.3)	RStudio Team, 2015	https://posit.co/; RRID:SCR_000432
clusterProfiler R package (v4.11.0)	Yu et al., 2012	https://bioconductor.org/packages/release/bioc/html/clusterProfiler.html; RRID:SCR_016884
ggplot2 package (v3.5.1)	Wickham, 2012	https://cran.r-project.org/web/packages/ggplot2/index.html; RRID:SCR_014601
Guitar R package (v2.14.0)	Cui et al., 2016	https://bioconductor.org/packages/release/bioc/html/Guitar.html
HOMER (v4.11)	Heinz et al., 2010	http://homer.ucsd.edu/; RRID:SCR_010881
FeatureCounts (v2.0.3)	Liao et al., 2014	http://subread.sourceforge.net/
VennDiagram (v 1.7.3)	Chen et al., 2011	https://cran.r-project.org/web/packages/VennDiagram/; RRID: SCR_002414
DESeq2 (v1.42.1)	Love et al., 2014	https://bioconductor.org/packages/release/bioc/html/DESeq2.html; RRID: SCR_015687
EEGLAB	wartz Center for Computational Neuroscience	https://sccn.ucsd.edu/eeglab/ EEGLAB; RRID:SCR_007292
MNE (v1.6.1)	Alexandre et al., 2013	http://martinos.org/mne/; RRID:SCR_005972
FOOOF toolbox (v1.1.0)	Donoghue et al., 2020	https://github.com/fooof-tools/fooof
Mobius software	Alpha MED Scientific	https://www.med64.com/products/med64-mobius-software/
Mobius offline toolkit software	Alpha MED Scientific	https://www.med64.com/products/med64-mobius-software/mobius-offline-toolkit/
pClamp 9 software	Molecular Devices	http://www.moleculardevices.com/products/software/pclamp.html; RRID:SCR_011323
MiniAnalysis software	Synaptosoft	http://www.synaptosoft.com/MiniAnalysis/; RRID:SCR_002184

NIS Elements (v5.42.06)	Nikon	https://www.nikoninstruments.com/Products/Software; RRID:SCR_014329
Imaris (v10.2.0)	Nikon	http://www.bitplane.com/imaris/imaris; RRID:SCR_007370
GraphPad Prism 6	GraphPad	https://www.graphpad.com/; RRID:SCR_002798
Python (v3.11.3)	Python Programming Language	https://www.python.org/; RRID:SCR_008394

818 **Figure legends**

819 **Figure 1. Synaptic malformations in FXS iPSC-derived cortical neurons. A**. Confocal
820 images of iPSC-derived neurons expressing neuronal markers DCX and TUJ1, cortical layer
821 markers BRN2, CTIP2, and TBR1, and the glutamatergic neuron marker CaMKII. The scale bar
822 is 50 μm. **B**. Quantification of neuronal, cortical layer, and glutamatergic marker expression.
823 Values represent mean ± s.e.m (n = 3 biological repeats per condition). **C-D**. Western blot
824 analysis and quantification of FMRP expression in iPSC-derived cortical neurons from
825 unaffected healthy controls (UHC) and FXS subjects. Values represent mean ± s.e.m. (n = 3 to
826 5 repeats per line; ***p < 0.001, two-tailed t-test). **E-F**. Western blot analysis and quantification
827 of synaptic proteins SV2 and Synapsin II expression in six-week-old UHC and FXS neurons.
828 Values represent mean ± s.e.m. (n = 3 to 5 repeats per line; **p < 0.01, ***p < 0.001, two-tailed
829 t-test). **G-H**. Representative images and quantification of synaptic puncta in six-week-old UHC
830 and FXS neurons stained for the synaptic markers SV2 and Synapsin II. The scale bar is 5 μm.
831 Values represent mean ± s.e.m. (n = 13 to 20 neurons per condition; ***p < 0.001, two-tailed t-
832 test). **I-K**. Illustration of mature and immature spines, confocal images, and quantification
833 showing an increase in the ratio of immature to mature spines in FXS iPSC-derived neurons
834 compared to controls. Arrows point to spines. The scale bar is 5 μm. Values represent mean ±
835 s.e.m. (n = 40 to 45 neurons per condition; ***p < 0.001, two-tailed t-test).

836

837 **Figure 2. Aberrant synaptic transmission, E/I imbalance, and hyperexcitability in FXS**
838 **iPSC-derived cortical neurons. A**. Phase image showing a six-week-old FXS iPSC-derived
839 neuron recorded via patch clamp. The scale bar is 50 μm. **B-D**. Defects in excitatory synaptic
840 transmission in FXS iPSC-derived cortical neurons compared to control neurons. Shown are
841 sample whole-cell voltage-clamp recording traces of excitatory postsynaptic currents (EPSCs)
842 from six-week-old neurons (**B**) and cumulative distribution plots of spontaneous EPSC intervals
843 (**C**, Kolmogorov–Smirnov test, the p-value is approaching zero.) and amplitudes (**D**,
844 Kolmogorov–Smirnov test, p < 2.2e-16). Insets display quantifications of mean frequencies and
845 amplitudes of spontaneous EPSCs. Values represent mean ± s.e.m. (n = 48 to 125 neurons per
846 condition; **p < 0.01, ***p < 0.001, two-tailed t-test). **E-G**. Defects in inhibitory synaptic
847 transmission in FXS iPSC-derived cortical neurons compared to control neurons. Shown are
848 sample whole-cell voltage-clamp traces of spontaneous inhibitory postsynaptic currents (IPSCs)
849 from six-week-old neurons (**E**, V_m = 20 mV), with cumulative distribution plots of spontaneous
850 IPSC intervals (**F**, Kolmogorov–Smirnov test, the p-value is approaching zero.) and amplitudes
851 (**G**, Kolmogorov–Smirnov test, the p-value is approaching zero.). Quantifications of mean

852 frequencies and amplitudes of spontaneous IPSCs are also shown. Values represent mean ±
853 s.e.m. (n = 40 to 58 neurons per condition; ***p < 0.001, two-tailed t-test). **H-L**. Increased
854 excitability in FXS iPSC-derived cortical neurons compared to control neurons. Sample whole-
855 cell current-clamp traces of evoked action potentials (APs) after a 60-pA injection in six-week-
856 old neurons (**H**), with quantifications of evoked AP frequency against injected current (**I**), and
857 threshold (**J**). Sample traces of spontaneous APs (**K**) and quantification of spontaneous AP
858 frequency (**L**) are also provided. Values represent mean ± s.e.m. (n = 45 to 49 neurons per
859 condition; *p < 0.05, **p < 0.01, ***p < 0.001, n.s. denotes non-significant; two-tailed t-test for
860 threshold and spontaneous AP frequency, two-way ANOVA with Tukey's multiple comparisons
861 for evoked AP frequency against injected current).
862
863 **Figure 3. Hyperexcitability and hyperconnectivity conserved between FXS iPSC model**
864 **and the same FXS subject. A**. Schematic illustrating electrophysiological workflows for MEA
865 and EEG recordings in both FXS subjects and their derived neurons. **B-E**. Increased excitability
866 in FXS iPSC-derived cortical neurons compared to control neurons. Shown are sample MEA
867 recording traces of spontaneous spikes from six-week-old neurons (**B**; right panel is an enlarged
868 view of dashed lines in the left panel) and cumulative distribution plots of spontaneous spike
869 intervals (**C**, Kolmogorov–Smirnov test, the p-value is approaching zero.). Quantifications of
870 mean inter-spike interval (Inset), burst duration (**D**), and spikes per burst (**E**) are provided.
871 Values represent mean ± s.e.m. (n = 3 cultures; ***p < 0.001, two-tailed t-test). **F-J**. Enhanced
872 network synchrony and hyperconnectivity in FXS iPSC-derived cortical circuitry compared to
873 controls. **F**. Sample traces and raster plots show array-wide spike detection rate (ASDR) across
874 64 electrodes over 120 seconds. Grey lines indicate network burst detection thresholds, black
875 boxes indicate burst duration, and color codes represent spike frequency. Quantifications of
876 network burst duration (**G**), active electrodes per network burst (**H**), network burst peak (**I**), and
877 spikes per network burst (**J**) are also shown. Values represent mean ± s.e.m. (n = 3 cultures;
878 ***p < 0.001, two-tailed t-test). **K-L**. Prolonged depolarization in FXS iPSC-derived cortical
879 circuitry compared to controls. Shown are sample traces of MEA recording sum amplitude over
880 64 electrodes across 70 seconds in control and FXS cortical circuitry (**K**). Dashed lines indicate
881 thresholds for UP-state detection, with boxes representing UP-state duration. Quantification of
882 UP-state duration is also shown (**L**). Values represent mean ± s.e.m. (n = 3 cultures; ***p <
883 0.001, two-tailed t-test). **M-N**. Cortical hyperactivity and hyperconnectivity in FXS patients.
884 Quantification of absolute power spectral density (PSD) across different frequency bands from
885 EEG data of four typically developing control (TDC) and FXS subjects (**M**). FOOOF (Fitting

886 Oscillations and One-Over-F) plot shows a steeper slope in FXS patients compared to TDC
887 subjects (**N**).
888
889 **Figure 4. FMRP binding to mRNAs encoding m^{6}A writers and the impact of FMRP**
890 **deficiency on writer expression. A**. Elevated m^{6}A levels in FXS iPSC-derived cortical neurons
891 compared to controls. Shown are dot blot assay results for polyA$^+$ RNA m^{6}A levels, with
892 quantification of m^{6}A intensity in FXS iPSC-derived neurons relative to controls, normalized to
893 methylene blue. Values represent mean ± s.e.m. (n = 4 cultures; **p < 0.01; two-tailed t-test). **B**.
894 Transcriptional expression analysis revealing no significant change of METTL3, METTL14, and
895 WTAP transcripts between control and FXS iPSCs-derived neurons. Values represent mean ±
896 s.e.m. (n = 7 control and 6 FXS samples; n.s. denotes non-significant; two-tailed t-test). **C-D**.
897 Western blot analysis and quantification of METTL3, METTL14, and WTAP protein levels.
898 Values represent mean ± s.e.m. (n = 4 cultures; *p < 0.05, **p < 0.01; two-tailed t-test). **E-F**.
899 FMRP binds to mRNAs encoding m^{6}A writers in HEK293T cells. Western blot of flag
900 immunoprecipitation with flag-tagged mCherry–FMRP and flag-tagged mCherry, along with their
901 input samples (**E**). Detection was performed with FMRP and GAPDH antibodies. RT-PCR
902 quantification of GAPDH, METTL3, METTL14, and WTAP mRNA enrichment in pulldown
903 samples (**F**) shows FMRP binding to METTL3, METTL14, and WTAP but not GAPDH mRNAs.
904 Values represent mean ± s.e.m. (n = three biological replicates; ***p < 0.001, n.s. denotes non-
905 significant; two-tailed t-test). **G**. RT-PCR quantification of METTL3, METTL14, and WTAP
906 mRNAs in translationally active heavy polysome fractions from FXS iPSC-derived neurons
907 versus controls. Values represent mean ± s.e.m. (n = 3 biological replicates; *p < 0.05, **p <
908 0.01; two-tailed test). **H**. Polysome profiles demonstrated a profound increase of global
909 translation, as indicated with a 23.5% increase in the ratio of heavy polysomes to monosomes
910 fractions (insert).
911
912 **Figure 5. Transcriptome-wide m^{6}A dysregulation in FXS iPSC-derived cortical neurons. A-**
913 **C**. Transcriptome-wide profiling of m^{6}A in 6-week-old neurons from healthy controls and FXS
914 patients. **A**. Metagene plot showing the distribution of m^{6}A peaks across human chromosomes.
915 **B**. Sequence logo illustrating the top enriched motif in m^{6}A peaks (p-value = 10^{-28}). **C**.
916 Distribution of m^{6}A methylation along transcripts, divided into 5′ UTR, CDS, and 3′ UTR. **D**.
917 Volcano plot depicting MeRIP-seq data for m^{6}A peaks differentially methylated between FXS
918 and control groups (n = 7 healthy controls, 6 FXS samples; adjusted p-value < 0.05; blue and
919 red dots represent significant hypo- and hyper-methylated sites). **E-F**. Histogram showing the

920 distribution of hyper- and hypo-methylated sites per gene (**E**) and per chromosome length
921 across human chromosomes (**F**; blue and red boxes indicate hypo- and hyper-methylated sites).
922 **G**. Gene Ontology (GO) analysis of differentially methylated genes (DMGs) between FXS iPSC-
923 derived neurons and controls, revealing the top 15 enriched cellular component (CC) and
924 biological process (BP) terms. The color represents the adjusted p-value, and the size
925 represents the gene ratio (percentage of DMGs in each GO term). **H**. Integrative Genomics
926 Viewer (IGV) tracks displaying MeRIP-seq read distribution for SYT3 and SYT5 mRNAs. **I-K**.
927 Venn diagrams showing overlap between hypermethylated transcripts and FMRP target
928 transcripts (**I**), SFARI ASD genes (**J**), and reported synapse-related genes (**K**), along with
929 representation factors and p-values. **L-M**. GO term analysis of genes overlapping between
930 hypermethylated transcripts and FMRP targets (**L**), as well as genes overlapping with SAFRI
931 ASD genes (**M**).
932
933 **Figure 6. Correlation of hypermethylation with gene downregulation and increased mRNA**
934 **decay in synapse-related genes. A**. Volcano plot displaying differential gene expression
935 between FXS iPSC-derived neurons and controls (n = 7 healthy controls, 6 FXS samples; fold
936 change > 1.4, p-value < 0.05; blue and red dots represent significantly down- and up-regulated
937 genes, respectively). **B**. Transcriptional expression analysis revealing significant abundant
938 FMR1 transcripts in control but not FXS iPSCs-derived neurons. Values are shown as mean ±
939 s.e.m. (n = 7 control, 6 FXS samples; *** p < 0.001; two-tailed t-test). **C**. Gene Ontology (GO)
940 term analysis of differentially expressed genes (DEGs) between FXS iPSC-derived neurons and
941 controls, showing the top 15 enrichment terms for cellular component (CC) and molecular
942 function (MF). The color indicates the adjusted P-value, and the size indicates the gene ratio
943 (percentage of total DEGs in each GO term). **D**. Conjoint analysis reveals a strong negative
944 correlation between m^6A modifications and gene expression levels (R = -0.47, p-value = 3.55e-
945 53, Chi-squared test), with a predominant hyper-down pattern in quadrant II (64.6% of total
946 correlations, indicating hyper-methylation paired with gene downregulation). **E**. GO term
947 analysis of hyper-methylated and downregulated transcripts. **F**. mRNA stability assay in FXS
948 iPSC-derived neurons and controls. RNA was isolated at designated time points following
949 actinomycin D treatment, and the stability of STY7 mRNAs was assessed by RT-qPCR (n = 3;
950 *** p < 0.001; two-tailed t-test).**G**. IGV tracks showing MeRIP-seq and RNA-seq read distribution
951 for STY7 mRNAs.
952

953 **Figure 7. Restoration of synaptic and neuronal functions in FXS iPSC-derived cortical**
954 **neurons. A**. MeRIP-qPCR analysis showing relative enrichment of m^6A modifications on
955 synapse-related mRNAs in control and FXS iPSC-derived cortical neurons, with and without
956 STM-2457 treatment. Values represent mean ± s.e.m. (n = 4 biological replicates; *p < 0.05,
957 ***p < 0.001, n.s. denotes non-significant; one-way ANOVA with Tukey's multiple comparisons.).
958 **B**. mRNA stability assay in FXS iPSC-derived neurons and controls, with and without STM-2457
959 treatment. RNA was isolated at specified time points after actinomycin D treatment, and the
960 stability of LRRC4B mRNAs was assessed via RT-qPCR. Values represent mean ± s.e.m. (n =
961 3 biological replicates; ***p < 0.001, n.s. denotes non-significant, one-way ANOVA with Tukey's
962 multiple comparisons.). **C-D**. Representative images and quantification of six-week-old control
963 and FXS neurons, with and without STM-2457 treatment, stained for the synaptic marker
964 Synapsin II. The scale bar is 5 μm. Values represent mean ± s.e.m. (n =10 to 20 neurons per
965 condition; ***p < 0.001, n.s. denotes non-significant; one-way ANOVA with Tukey's multiple
966 comparisons). **E-F**. Sample whole-cell voltage-clamp recordings of excitatory postsynaptic
967 currents (EPSCs) in six-week-old neurons, with and without STM-2457 treatment (**E**), and
968 quantification of mean spontaneous EPSC frequencies (**F**). Values are presented as mean ±
969 s.e.m. (n = 6 to 10 neurons per condition; ***p < 0.001, n.s. denotes non-significant; one-way
970 ANOVA with Tukey's multiple comparisons). **G-H**. Whole-cell current-clamp recordings of
971 evoked action potentials (APs) (**G**), and their quantification (**H**). Values are presented as mean ±
972 s.e.m. (n = 5 to 8 neurons per condition; *p < 0.05, n.s. denotes non-significant; two-way
973 ANOVA with Tukey's multiple comparisons).
974
975
976 **Supplemental Figure legends**
977 **Supplemental Figure 1. Modeling FXS using patient-derived iPSCs. A**. Electropherogram of
978 Asuragen test results showing 29 CGG repeats in UHC-5 and a full mutation with over 200 CGG
979 repeats in FXS-5 iPSC lines. **B**. Confocal images of iPSC-derived neural progenitors expressing
980 markers such as Nestin, Sox2, ZO1, FOXG1, PAX6, and OTX2. The scale bar is 50 μm. **C**.
981 Quantification of neural progenitor marker expression. Values represent mean ± s.e.m. (n = 5 to
982 76 neurons per condition). **D-L**. Semi-automated Sholl analysis reveals no significant
983 differences in neurite parameters between FXS patient-derived cortical neurons and control
984 neurons. Shown are representative images of GFP-labeled FXS and control neurons (**D**), a
985 schematic of neurite analysis (**E**), and quantification of neurite parameters including number of
986 sections (**F**), total neurite length (**G**), terminal points (**H**), branch points (**I**), maximum section

length (**J**), minimum section length (**K**), and mean section length (**L**). The scale bar is 50 μm. Values represent mean ± s.e.m. (n = 30 to 169 neurons per condition; n.s. denotes non-significance; two-tailed t-test).

Supplemental Figure 2. Sodium and potassium channel activity. A-B. Quantification of evoked action potential (AP) amplitude (**A**) and rheobase (**B**). Values are presented as mean ± s.e.m. (n = 43 to 92 neurons per condition; n.s. denotes non-significance; two-tailed t-test). **C-E**. Sample whole-cell voltage-clamp recording traces of sodium and potassium channel activity (**C**), along with quantification of sodium (**D**) and potassium (**E**) currents. Values are presented as mean ± s.e.m. (n = 56 to 107 neurons per condition; n.s. denotes non-significance; two-tailed t-test).

Supplemental Figure 3. MEA and EEG recordings. A. Sample bright-field images of human cortical neuron cultures at 6 weeks post-neuronal differentiation. The scale bar is 50 μm. **B-C**. Increased waveforms detected per electrode by automatic spiking sorting in FXS cortical microcircuitry compared to controls. Shown are sample waveforms for electrode 6 and 26 in control and FXS iPSCs-derived cortical microcircuitry (**B**). Quantification of waveforms per channel is also presented (**C**). Values represent mean ± s.e.m. (n = 3 cultures; ***$p < 0.001$; two-tailed t-test). **D**. Power spectral density (PSD) traces across different frequency bands from four typically developing control (TDC) and FXS subjects' EEG data. Numbers indicate TDC and FXS experimental IDs.

Supplemental Figure 4. Elevated m^6A levels associated with increased m^6A writer expression in *Fmr1* knockout mice. A. Increased m^6A levels in *Fmr1* knockout mice compared to wild type (WT) mice. Shown are dot blot assays of $polyA^+$ RNA m^6A levels and quantification of m^6A intensity in *Fmr1* knockout neurons relative to WT, normalized to methylene blue (n = 4 samples; ***$p < 0.001$; two-tailed t-test). **B**. Transcriptional expression analysis revealing no significant change of METTL3, METTL14, and WTAP transcripts from RNA sequencing between WT and *Fmr1* knockout mice. Values represent mean ± s.e.m. (n = 2 wild type and 2 *Fmr1* knockout mice; n.s. denotes non-significance; two-tailed t-test). **C-D**. Western blot analysis and quantification of FMRP, METTL3, and WTAP protein levels. Values represent mean ± s.e.m. (n = 4 samples; ***$p < 0.001$; two-tailed t-test).

1020 **Supplemental Figure 5. Transcriptome-wide m^6A dysregulation in postmortem brain**
1021 **tissues from FXS subjects. A-C**. Transcriptome-wide m^6A profiling in postmortem brain tissue
1022 (Brodmann area 44) derived from FXS subjects and healthy controls. **A**. Metagene plot showing
1023 m^6A peak distribution across human chromosomes. **B**. Sequence logo depicting the top
1024 enriched motif in m^6A peaks (p value = 10^{-4}). **C**. Distribution of m^6A methylation across
1025 transcripts, with each transcript divided into 5′ UTR, CDS, and 3′ UTR. **D**. Volcano plot
1026 displaying MeRIP-seq data of differentially methylated m^6A peaks between FXS and control
1027 groups (n = 3 healthy controls and 3 FXS samples; adjusted p-value < 0.01; blue and red dots
1028 indicate significant hypo- and hyper-methylated sites, respectively). **E-F**. Histogram illustrating
1029 the distribution of hypo- and hyper-methylated sites per gene (**E**) and per chromosome length
1030 (**F**), with blue and red boxes indicating hypo- and hyper-methylated sites, respectively. **G**. Gene
1031 Ontology (GO) term analysis of differentially methylated genes (DMGs) between FXS subjects
1032 and controls, showing top 15 enrichment terms for cellular component (CC) and biological
1033 process (BP). The color represents the adjusted P-value, and the size of the shape represents
1034 the gene ratio (percentage of total DMGs in the given GO term). **H-J**. Venn diagrams showing
1035 the overlap between hypermethylated transcripts and FMRP target transcripts (**H**), SFARI ASD
1036 genes (**I**), and reported synapse-related genes (**J**), along with representation factors and p-
1037 values. **K-L**. GO term analysis of overlapped genes between hypermethylated transcripts and
1038 FMRP target transcripts (**K**) and between hypermethylated transcripts and SFARI ASD genes
1039 (**L**).
1040
1041 **Supplemental Figure 6. Correlation of hypermethylation with gene downregulation in**
1042 **postmortem brain tissues from FXS subjects. A**. Venn diagram, drawn to scale, shows the
1043 overlap between differentially expressed genes (DEGs) in FXS iPSCs-derived neurons and
1044 controls, and FMRP target transcripts, with representation factor and P-value. **B**. Gene Ontology
1045 (GO) term analysis of overlapped genes between hypermethylated transcripts and FMRP target
1046 transcripts reveals the top 15 enriched terms for cellular component (CC) and biological process
1047 (BP). The color represents the adjusted p-value, and the size represents the gene ratio,
1048 indicating the percentage of total DMGs within each GO term. **C**. Venn diagram shows the
1049 overlap between DEGs and reported synaptic genes, with representation factor and P-value. **D**.
1050 Volcano plot illustrating differential gene expression analysis in postmortem brain tissue
1051 (Brodmann area 44) from FXS subjects versus healthy controls (n = 3 healthy controls and 3
1052 FXS samples; fold change > 1.4, p-value < 0.05; blue and red dots represent significantly down-
1053 and up-regulated genes, respectively). **E-F**. Venn diagrams show the overlap between DEGs

1054 from postmortem tissues and FMRP target transcripts (**E**) and SFARI ASD genes (**F**), along with
1055 representation factors and P-values. **G-H**. GO term analysis of overlapped genes between
1056 DEGs and FMRP target transcripts (**G**), as well as DEGs and SFARI ASD genes (**H**), revealing
1057 the top 15 enriched terms for cellular component (CC), biological process (BP), and molecular
1058 function (MF). **I**. Venn diagram illustrating the overlap between DEGs from postmortem tissues
1059 and reported synaptic genes, with the representation factor and P-value. **J**. Conjoint analysis
1060 shows a strong negative correlation between m^6A modifications and gene expression levels
1061 from postmortem brain tissues (R = -0.33, p-value = 1.152e-53, Chi-squared test), with a
1062 notable hyper-down pattern in quadrant II (hyper-methylation paired with gene downregulation,
1063 72.9% of total correlations). **K**. GO term analysis of transcripts with hyper-methylation paired
1064 with gene downregulation.

1065 **Reference**

1066 1. Bear, M.F., Huber, K.M., and Warren, S.T. (2004). The mGluR theory of fragile X mental
1067 retardation. Trends Neurosci *27*, 370-377. 10.1016/j.tins.2004.04.009.
1068 2. Dolen, G., and Bear, M.F. (2008). Role for metabotropic glutamate receptor 5 (mGluR5)
1069 in the pathogenesis of fragile X syndrome. J Physiol *586*, 1503-1508.
1070 10.1113/jphysiol.2008.150722.
1071 3. Nelson, S.B., and Valakh, V. (2015). Excitatory/Inhibitory Balance and Circuit Homeostasis
1072 in Autism Spectrum Disorders. Neuron *87*, 684-698. 10.1016/j.neuron.2015.07.033.
1073 4. Gibson, J.R., Bartley, A.F., Hays, S.A., and Huber, K.M. (2008). Imbalance of neocortical
1074 excitation and inhibition and altered UP states reflect network hyperexcitability in the
1075 mouse model of fragile X syndrome. J Neurophysiol *100*, 2615-2626.
1076 10.1152/jn.90752.2008.
1077 5. Gao, R., and Penzes, P. (2015). Common mechanisms of excitatory and inhibitory
1078 imbalance in schizophrenia and autism spectrum disorders. Curr Mol Med *15*, 146-167.
1079 10.2174/1566524015666150303003028.
1080 6. Contractor, A., Klyachko, V.A., and Portera-Cailliau, C. (2015). Altered Neuronal and
1081 Circuit Excitability in Fragile X Syndrome. Neuron *87*, 699-715.
1082 10.1016/j.neuron.2015.06.017.
1083 7. Berry-Kravis, E.M., Lindemann, L., Jonch, A.E., Apostol, G., Bear, M.F., Carpenter, R.L.,
1084 Crawley, J.N., Curie, A., Des Portes, V., Hossain, F., et al. (2018). Drug development for
1085 neurodevelopmental disorders: lessons learned from fragile X syndrome. Nat Rev Drug
1086 Discov *17*, 280-299. 10.1038/nrd.2017.221.
1087 8. Erickson, C.A., Davenport, M.H., Schaefer, T.L., Wink, L.K., Pedapati, E.V., Sweeney, J.A.,
1088 Fitzpatrick, S.E., Brown, W.T., Budimirovic, D., Hagerman, R.J., et al. (2017). Fragile X
1089 targeted pharmacotherapy: lessons learned and future directions. J Neurodev Disord *9*,
1090 7. 10.1186/s11689-017-9186-9.
1091 9. Liu, X.S., Wu, H., Krzisch, M., Wu, X., Graef, J., Muffat, J., Hnisz, D., Li, C.H., Yuan, B., Xu,
1092 C., et al. (2018). Rescue of Fragile X Syndrome Neurons by DNA Methylation Editing of
1093 the FMR1 Gene. Cell *172*, 979-992 e976. 10.1016/j.cell.2018.01.012.
1094 10. Achuta, V.S., Moykkynen, T., Peteri, U.K., Turconi, G., Rivera, C., Keinanen, K., and
1095 Castren, M.L. (2018). Functional changes of AMPA responses in human induced
1096 pluripotent stem cell-derived neural progenitors in fragile X syndrome. Sci Signal *11*.
1097 10.1126/scisignal.aan8784.
1098 11. Zhang, Z., Marro, S.G., Zhang, Y., Arendt, K.L., Patzke, C., Zhou, B., Fair, T., Yang, N.,
1099 Sudhof, T.C., Wernig, M., and Chen, L. (2018). The fragile X mutation impairs homeostatic
1100 plasticity in human neurons by blocking synaptic retinoic acid signaling. Sci Transl Med
1101 *10*. 10.1126/scitranslmed.aar4338.
1102 12. Raj, N., McEachin, Z.T., Harousseau, W., Zhou, Y., Zhang, F., Merritt-Garza, M.E.,
1103 Taliaferro, J.M., Kalinowska, M., Marro, S.G., Hales, C.M., et al. (2021). Cell-type-specific
1104 profiling of human cellular models of fragile X syndrome reveal PI3K-dependent defects
1105 in translation and neurogenesis. Cell Rep *35*, 108991. 10.1016/j.celrep.2021.108991.
1106 13. Kang, Y., Zhou, Y., Li, Y., Han, Y., Xu, J., Niu, W., Li, Z., Liu, S., Feng, H., Huang, W., et al.
1107 (2021). A human forebrain organoid model of fragile X syndrome exhibits altered

1108 neurogenesis and highlights new treatment strategies. Nat Neurosci *24*, 1377-1391.
1109 10.1038/s41593-021-00913-6.
1110 14. Sharma, S.D., Reddy, B.K., Pal, R., Ritakari, T.E., Cooper, J.D., Selvaraj, B.T., Kind, P.C.,
1111 Chandran, S., Wyllie, D.J.A., and Chattarji, S. (2023). Astrocytes mediate cell non-
1112 autonomous correction of aberrant firing in human FXS neurons. Cell Rep *42*, 112344.
1113 10.1016/j.celrep.2023.112344.
1114 15. Geula, S., Moshitch-Moshkovitz, S., Dominissini, D., Mansour, A.A., Kol, N., Salmon-
1115 Divon, M., Hershkovitz, V., Peer, E., Mor, N., Manor, Y.S., et al. (2015). Stem cells. m6A
1116 mRNA methylation facilitates resolution of naive pluripotency toward differentiation.
1117 Science *347*, 1002-1006. 10.1126/science.1261417.
1118 16. Liu, J., Yue, Y., Han, D., Wang, X., Fu, Y., Zhang, L., Jia, G., Yu, M., Lu, Z., Deng, X., et al.
1119 (2014). A METTL3-METTL14 complex mediates mammalian nuclear RNA N6-adenosine
1120 methylation. Nat Chem Biol *10*, 93-95. 10.1038/nchembio.1432.
1121 17. Ping, X.L., Sun, B.F., Wang, L., Xiao, W., Yang, X., Wang, W.J., Adhikari, S., Shi, Y., Lv, Y.,
1122 Chen, Y.S., et al. (2014). Mammalian WTAP is a regulatory subunit of the RNA N6-
1123 methyladenosine methyltransferase. Cell Res *24*, 177-189. 10.1038/cr.2014.3.
1124 18. Horiuchi, K., Kawamura, T., Iwanari, H., Ohashi, R., Naito, M., Kodama, T., and Hamakubo,
1125 T. (2013). Identification of Wilms' tumor 1-associating protein complex and its role in
1126 alternative splicing and the cell cycle. J Biol Chem *288*, 33292-33302.
1127 10.1074/jbc.M113.500397.
1128 19. Patil, D.P., Chen, C.K., Pickering, B.F., Chow, A., Jackson, C., Guttman, M., and Jaffrey, S.R.
1129 (2016). m(6)A RNA methylation promotes XIST-mediated transcriptional repression.
1130 Nature *537*, 369-373. 10.1038/nature19342.
1131 20. Yang, Y., Hsu, P.J., Chen, Y.S., and Yang, Y.G. (2018). Dynamic transcriptomic m(6)A
1132 decoration: writers, erasers, readers and functions in RNA metabolism. Cell Res *28*, 616-
1133 624. 10.1038/s41422-018-0040-8.
1134 21. Jia, G., Fu, Y., Zhao, X., Dai, Q., Zheng, G., Yang, Y., Yi, C., Lindahl, T., Pan, T., Yang, Y.G.,
1135 and He, C. (2011). N6-methyladenosine in nuclear RNA is a major substrate of the
1136 obesity-associated FTO. Nat Chem Biol *7*, 885-887. 10.1038/nchembio.687.
1137 22. Zheng, G., Dahl, J.A., Niu, Y., Fedorcsak, P., Huang, C.M., Li, C.J., Vagbo, C.B., Shi, Y.,
1138 Wang, W.L., Song, S.H., et al. (2013). ALKBH5 is a mammalian RNA demethylase that
1139 impacts RNA metabolism and mouse fertility. Mol Cell *49*, 18-29.
1140 10.1016/j.molcel.2012.10.015.
1141 23. Jiang, X., Liu, B., Nie, Z., Duan, L., Xiong, Q., Jin, Z., Yang, C., and Chen, Y. (2021). The role
1142 of m6A modification in the biological functions and diseases. Signal Transduct Target
1143 Ther *6*, 74. 10.1038/s41392-020-00450-x.
1144 24. He, P.C., and He, C. (2021). m(6) A RNA methylation: from mechanisms to therapeutic
1145 potential. EMBO J *40*, e105977. 10.15252/embj.2020105977.
1146 25. Yue, Y., Liu, J., and He, C. (2015). RNA N6-methyladenosine methylation in post-
1147 transcriptional gene expression regulation. Genes Dev *29*, 1343-1355.
1148 10.1101/gad.262766.115.
1149 26. Weng, Y.L., Wang, X., An, R., Cassin, J., Vissers, C., Liu, Y., Liu, Y., Xu, T., Wang, X., Wong,
1150 S.Z.H., et al. (2018). Epitranscriptomic m(6)A Regulation of Axon Regeneration in the

Adult Mammalian Nervous System. Neuron *97*, 313-325 e316. 10.1016/j.neuron.2017.12.036.

27. Xu, H., Dzhashiashvili, Y., Shah, A., Kunjamma, R.B., Weng, Y.L., Elbaz, B., Fei, Q., Jones, J.S., Li, Y.I., Zhuang, X., et al. (2020). m(6)A mRNA Methylation Is Essential for Oligodendrocyte Maturation and CNS Myelination. Neuron *105*, 293-309 e295. 10.1016/j.neuron.2019.12.013.

28. Yoon, K.J., Ringeling, F.R., Vissers, C., Jacob, F., Pokrass, M., Jimenez-Cyrus, D., Su, Y., Kim, N.S., Zhu, Y., Zheng, L., et al. (2017). Temporal Control of Mammalian Cortical Neurogenesis by m(6)A Methylation. Cell *171*, 877-889 e817. 10.1016/j.cell.2017.09.003.

29. Livneh, I., Moshitch-Moshkovitz, S., Amariglio, N., Rechavi, G., and Dominissini, D. (2020). The m(6)A epitranscriptome: transcriptome plasticity in brain development and function. Nat Rev Neurosci *21*, 36-51. 10.1038/s41583-019-0244-z.

30. Shi, H., Zhang, X., Weng, Y.L., Lu, Z., Liu, Y., Lu, Z., Li, J., Hao, P., Zhang, Y., Zhang, F., et al. (2018). m(6)A facilitates hippocampus-dependent learning and memory through YTHDF1. Nature *563*, 249-253. 10.1038/s41586-018-0666-1.

31. Engel, M., Eggert, C., Kaplick, P.M., Eder, M., Roh, S., Tietze, L., Namendorf, C., Arloth, J., Weber, P., Rex-Haffner, M., et al. (2018). The Role of m(6)A/m-RNA Methylation in Stress Response Regulation. Neuron *99*, 389-403 e389. 10.1016/j.neuron.2018.07.009.

32. O'Roak, B.J., Vives, L., Girirajan, S., Karakoc, E., Krumm, N., Coe, B.P., Levy, R., Ko, A., Lee, C., Smith, J.D., et al. (2012). Sporadic autism exomes reveal a highly interconnected protein network of de novo mutations. Nature *485*, 246-250. 10.1038/nature10989.

33. Iossifov, I., Levy, D., Allen, J., Ye, K., Ronemus, M., Lee, Y.H., Yamrom, B., and Wigler, M. (2015). Low load for disruptive mutations in autism genes and their biased transmission. Proc Natl Acad Sci U S A *112*, E5600-5607. 10.1073/pnas.1516376112.

34. De Rubeis, S., He, X., Goldberg, A.P., Poultney, C.S., Samocha, K., Cicek, A.E., Kou, Y., Liu, L., Fromer, M., Walker, S., et al. (2014). Synaptic, transcriptional and chromatin genes disrupted in autism. Nature *515*, 209-215. 10.1038/nature13772.

35. Zhou, X., Feliciano, P., Shu, C., Wang, T., Astrovskaya, I., Hall, J.B., Obiajulu, J.U., Wright, J.R., Murali, S.C., Xu, S.X., et al. (2022). Integrating de novo and inherited variants in 42,607 autism cases identifies mutations in new moderate-risk genes. Nat Genet *54*, 1305-1319. 10.1038/s41588-022-01148-2.

36. Richter, J.D., and Zhao, X. (2021). The molecular biology of FMRP: new insights into fragile X syndrome. Nat Rev Neurosci *22*, 209-222. 10.1038/s41583-021-00432-0.

37. Darnell, J.C., and Klann, E. (2013). The translation of translational control by FMRP: therapeutic targets for FXS. Nat Neurosci *16*, 1530-1536. 10.1038/nn.3379.

38. Darnell, J.C., Van Driesche, S.J., Zhang, C., Hung, K.Y., Mele, A., Fraser, C.E., Stone, E.F., Chen, C., Fak, J.J., Chi, S.W., et al. (2011). FMRP stalls ribosomal translocation on mRNAs linked to synaptic function and autism. Cell *146*, 247-261. 10.1016/j.cell.2011.06.013.

39. Zalfa, F., Giorgi, M., Primerano, B., Moro, A., Di Penta, A., Reis, S., Oostra, B., and Bagni, C. (2003). The fragile X syndrome protein FMRP associates with BC1 RNA and regulates the translation of specific mRNAs at synapses. Cell *112*, 317-327. 10.1016/s0092-8674(03)00079-5.

40. Edupuganti, R.R., Geiger, S., Lindeboom, R.G.H., Shi, H., Hsu, P.J., Lu, Z., Wang, S.Y., Baltissen, M.P.A., Jansen, P., Rossa, M., et al. (2017). N(6)-methyladenosine (m(6)A)

1195 recruits and repels proteins to regulate mRNA homeostasis. Nat Struct Mol Biol *24*, 870-
1196 878. 10.1038/nsmb.3462.
1197 41. Chang, M., Lv, H., Zhang, W., Ma, C., He, X., Zhao, S., Zhang, Z.W., Zeng, Y.X., Song, S., Niu,
1198 Y., and Tong, W.M. (2017). Region-specific RNA m(6)A methylation represents a new
1199 layer of control in the gene regulatory network in the mouse brain. Open Biol *7*.
1200 10.1098/rsob.170166.
1201 42. Arguello, A.E., DeLiberto, A.N., and Kleiner, R.E. (2017). RNA Chemical Proteomics
1202 Reveals the N(6)-Methyladenosine (m(6)A)-Regulated Protein-RNA Interactome. J Am
1203 Chem Soc *139*, 17249-17252. 10.1021/jacs.7b09213.
1204 43. Edens, B.M., Vissers, C., Su, J., Arumugam, S., Xu, Z., Shi, H., Miller, N., Rojas Ringeling, F.,
1205 Ming, G.L., He, C., et al. (2019). FMRP Modulates Neural Differentiation through m(6)A-
1206 Dependent mRNA Nuclear Export. Cell Rep *28*, 845-854 e845.
1207 10.1016/j.celrep.2019.06.072.
1208 44. Hsu, P.J., Shi, H., Zhu, A.C., Lu, Z., Miller, N., Edens, B.M., Ma, Y.C., and He, C. (2019). The
1209 RNA-binding protein FMRP facilitates the nuclear export of N(6)-methyladenosine-
1210 containing mRNAs. J Biol Chem *294*, 19889-19895. 10.1074/jbc.AC119.010078.
1211 45. Zou, Z., Wei, J., Chen, Y., Kang, Y., Shi, H., Yang, F., Shi, Z., Chen, S., Zhou, Y., Sepich-Poore,
1212 C., et al. (2023). FMRP phosphorylation modulates neuronal translation through YTHDF1.
1213 Mol Cell *83*, 4304-4317 e4308. 10.1016/j.molcel.2023.10.028.
1214 46. Worpenberg, L., Paolantoni, C., Longhi, S., Mulorz, M.M., Lence, T., Wessels, H.H., Dassi,
1215 E., Aiello, G., Sutandy, F.X.R., Scheibe, M., et al. (2021). Ythdf is a N6-methyladenosine
1216 reader that modulates Fmr1 target mRNA selection and restricts axonal growth in
1217 Drosophila. EMBO J *40*, e104975. 10.15252/embj.2020104975.
1218 47. Zhang, F., Kang, Y., Wang, M., Li, Y., Xu, T., Yang, W., Song, H., Wu, H., Shu, Q., and Jin, P.
1219 (2018). Fragile X mental retardation protein modulates the stability of its m6A-marked
1220 messenger RNA targets. Hum Mol Genet *27*, 3936-3950. 10.1093/hmg/ddy292.
1221 48. Bagni, C., and Zukin, R.S. (2019). A Synaptic Perspective of Fragile X Syndrome and
1222 Autism Spectrum Disorders. Neuron *101*, 1070-1088. 10.1016/j.neuron.2019.02.041.
1223 49. Zhang, A., Sokolova, I., Domissy, A., Davis, J., Rao, L., Hana Utami, K., Wang, Y.,
1224 Hagerman, R.J., Pouladi, M.A., Sanna, P., et al. (2022). Maturation Delay of Human
1225 GABAergic Neurogenesis in Fragile X Syndrome Pluripotent Stem Cells. Stem Cells Transl
1226 Med *11*, 613-629. 10.1093/stcltm/szac022.
1227 50. Das Sharma, S., Pal, R., Reddy, B.K., Selvaraj, B.T., Raj, N., Samaga, K.K., Srinivasan, D.J.,
1228 Ornelas, L., Sareen, D., Livesey, M.R., et al. (2020). Cortical neurons derived from human
1229 pluripotent stem cells lacking FMRP display altered spontaneous firing patterns. Mol
1230 Autism *11*, 52. 10.1186/s13229-020-00351-4.
1231 51. Pfeiffer, B.E., and Huber, K.M. (2009). The state of synapses in fragile X syndrome.
1232 Neuroscientist *15*, 549-567. 10.1177/1073858409333075.
1233 52. Pedapati, E.V., Schmitt, L.M., Ethridge, L.E., Miyakoshi, M., Sweeney, J.A., Liu, R., Smith,
1234 E., Shaffer, R.C., Dominick, K.C., Gilbert, D.L., et al. (2022). Neocortical localization and
1235 thalamocortical modulation of neuronal hyperexcitability contribute to Fragile X
1236 Syndrome. Commun Biol *5*, 442. 10.1038/s42003-022-03395-9.

1237 53. Smith, E.G., Pedapati, E.V., Liu, R., Schmitt, L.M., Dominick, K.C., Shaffer, R.C., Sweeney,
1238 J.A., and Erickson, C.A. (2021). Sex differences in resting EEG power in Fragile X
1239 Syndrome. J Psychiatr Res *138*, 89-95. 10.1016/j.jpsychires.2021.03.057.
1240 54. Schmitt, L.M., Li, J., Liu, R., Horn, P.S., Sweeney, J.A., Erickson, C.A., and Pedapati, E.V.
1241 (2022). Altered frontal connectivity as a mechanism for executive function deficits in
1242 fragile X syndrome. Mol Autism *13*, 47. 10.1186/s13229-022-00527-0.
1243 55. Ethridge, L.E., White, S.P., Mosconi, M.W., Wang, J., Pedapati, E.V., Erickson, C.A., Byerly,
1244 M.J., and Sweeney, J.A. (2017). Neural synchronization deficits linked to cortical hyper-
1245 excitability and auditory hypersensitivity in fragile X syndrome. Mol Autism *8*, 22.
1246 10.1186/s13229-017-0140-1.
1247 56. Gerster, M., Waterstraat, G., Litvak, V., Lehnertz, K., Schnitzler, A., Florin, E., Curio, G.,
1248 and Nikulin, V. (2022). Separating Neural Oscillations from Aperiodic 1/f Activity:
1249 Challenges and Recommendations. Neuroinformatics *20*, 991-1012. 10.1007/s12021-
1250 022-09581-8.
1251 57. Donoghue, T., Haller, M., Peterson, E.J., Varma, P., Sebastian, P., Gao, R., Noto, T., Lara,
1252 A.H., Wallis, J.D., Knight, R.T., et al. (2020). Parameterizing neural power spectra into
1253 periodic and aperiodic components. Nat Neurosci *23*, 1655-1665. 10.1038/s41593-020-
1254 00744-x.
1255 58. Gross, C., Nakamoto, M., Yao, X., Chan, C.B., Yim, S.Y., Ye, K., Warren, S.T., and Bassell,
1256 G.J. (2010). Excess phosphoinositide 3-kinase subunit synthesis and activity as a novel
1257 therapeutic target in fragile X syndrome. J Neurosci *30*, 10624-10638.
1258 10.1523/JNEUROSCI.0402-10.2010.
1259 59. Cao, Y., Ye, Q., Ma, M., and She, Q.B. (2023). Enhanced bypass of PD-L1 translation
1260 reduces the therapeutic response to mTOR kinase inhibitors. Cell Rep *42*, 112764.
1261 10.1016/j.celrep.2023.112764.
1262 60. Yankova, E., Blackaby, W., Albertella, M., Rak, J., De Braekeleer, E., Tsagkogeorga, G.,
1263 Pilka, E.S., Aspris, D., Leggate, D., Hendrick, A.G., et al. (2021). Small-molecule inhibition
1264 of METTL3 as a strategy against myeloid leukaemia. Nature *593*, 597-601.
1265 10.1038/s41586-021-03536-w.
1266 61. Richter, J.D., Bassell, G.J., and Klann, E. (2015). Dysregulation and restoration of
1267 translational homeostasis in fragile X syndrome. Nat Rev Neurosci *16*, 595-605.
1268 10.1038/nrn4001.
1269 62. Sansone, S.M., Schneider, A., Bickel, E., Berry-Kravis, E., Prescott, C., and Hessl, D. (2014).
1270 Improving IQ measurement in intellectual disabilities using true deviation from
1271 population norms. J Neurodev Disord *6*, 16. 10.1186/1866-1955-6-16.
1272 63. Boggs, A.E., Schmitt, L.M., McLane, R.D., Adayev, T., LaFauci, G., Horn, P.S., Dominick,
1273 K.C., Gross, C., and Erickson, C.A. (2022). Optimization, validation and initial clinical
1274 implications of a Luminex-based immunoassay for the quantification of Fragile X Protein
1275 from dried blood spots. Sci Rep *12*, 5617. 10.1038/s41598-022-09633-8.
1276 64. Straub, D., Schmitt, L.M., Boggs, A.E., Horn, P.S., Dominick, K.C., Gross, C., and Erickson,
1277 C.A. (2023). A sensitive and reproducible qRT-PCR assay detects physiological relevant
1278 trace levels of FMR1 mRNA in individuals with Fragile X syndrome. Sci Rep *13*, 3808.
1279 10.1038/s41598-023-29786-4.

1280 65. Dao, L., You, Z., Lu, L., Xu, T., Sarkar, A.K., Zhu, H., Liu, M., Calandrelli, R., Yoshida, G., Lin,
1281 P., et al. (2024). Modeling blood-brain barrier formation and cerebral cavernous
1282 malformations in human PSC-derived organoids. Cell Stem Cell.
1283 10.1016/j.stem.2024.04.019.
1284 66. Wen, Z., Nguyen, H.N., Guo, Z., Lalli, M.A., Wang, X., Su, Y., Kim, N.S., Yoon, K.J., Shin, J.,
1285 Zhang, C., et al. (2014). Synaptic dysregulation in a human iPS cell model of mental
1286 disorders. Nature *515*, 414-418. 10.1038/nature13716.
1287 67. Shi, Y., Kirwan, P., and Livesey, F.J. (2012). Directed differentiation of human pluripotent
1288 stem cells to cerebral cortex neurons and neural networks. Nat Protoc *7*, 1836-1846.
1289 10.1038/nprot.2012.116.
1290 68. Qi, Y., Zhang, X.J., Renier, N., Wu, Z., Atkin, T., Sun, Z., Ozair, M.Z., Tchieu, J., Zimmer, B.,
1291 Fattahi, F., et al. (2017). Combined small-molecule inhibition accelerates the derivation
1292 of functional cortical neurons from human pluripotent stem cells. Nat Biotechnol *35*,
1293 154-163. 10.1038/nbt.3777.
1294 69. Guler, B.E., Krzysko, J., and Wolfrum, U. (2021). Isolation and culturing of primary mouse
1295 astrocytes for the analysis of focal adhesion dynamics. STAR Protoc *2*, 100954.
1296 10.1016/j.xpro.2021.100954.
1297 70. Hays, S.A., Huber, K.M., and Gibson, J.R. (2011). Altered neocortical rhythmic activity
1298 states in Fmr1 KO mice are due to enhanced mGluR5 signaling and involve changes in
1299 excitatory circuitry. J Neurosci *31*, 14223-14234. 10.1523/JNEUROSCI.3157-11.2011.
1300 71. Delorme, A., and Makeig, S. (2004). EEGLAB: an open source toolbox for analysis of
1301 single-trial EEG dynamics including independent component analysis. J Neurosci
1302 Methods *134*, 9-21. 10.1016/j.jneumeth.2003.10.009.
1303

Acknowledgements: We would like to thank to the members of Guo Laboratory, Dr. Chuan He, as well as Drs. Aaron Zorn, James Well, and Kenneth Campbell, for their valuable comments and suggestions. We also thank Dr. Andrew Volk for providing the WTAP antibody. This study has received support from the National Institutes of Health (NIH) grants (R21NS122169 and R21MH132038), the Cincinnati Children's Hospital Medical Center (CCHMC) Trustee Grant Award, and the Local Initiative for Excellence Foundation to Dr. Ziyuan Guo. The NIH grant R01NS115507 and Department of Veteran Affairs grants I01BX002149 and IK6BX006316 to Dr. Haining Zhu are acknowledged. We would also like to express our gratitude to NIH NeuroBioBank for providing human postmortem brain tissues.

Author Contributions: Author Contributions: L.L. led and was involved in every aspect of the project. A.S. conducted whole-cell patch-clamp recording and analysis. L.D., X.C., and J.T. contributed to cell cultures and immunostaining. J.L., M.M., and E.P. conducted EEG analysis. C.M., P.T., and H.Z. performed polysome profiling analysis. G.Y., A.L., and C.W made contributions to data analysis. C.W., L.S., and C.E. provided clinical samples and data. M.C. and M.S. carried out Asuragen testing. Y.Z. contributed to MEA analysis. Y.L. and N.S. made contributions to MeRIP sequencing and RNA sequencing analysis. X.W., L.Z., and D.L. contributed to experimental design. C.G. made contributions to immunoprecipitation experiments and provide *Fmr1* knockout brains. Z.G. conceptualized and designed the project and wrote the manuscript.

Author information: MeRIP sequencing and RNA sequencing data were deposit at GEO. Correspondence and requests for materials should be address to Z.G. (Ziyuan.Guo@cchmc.org).

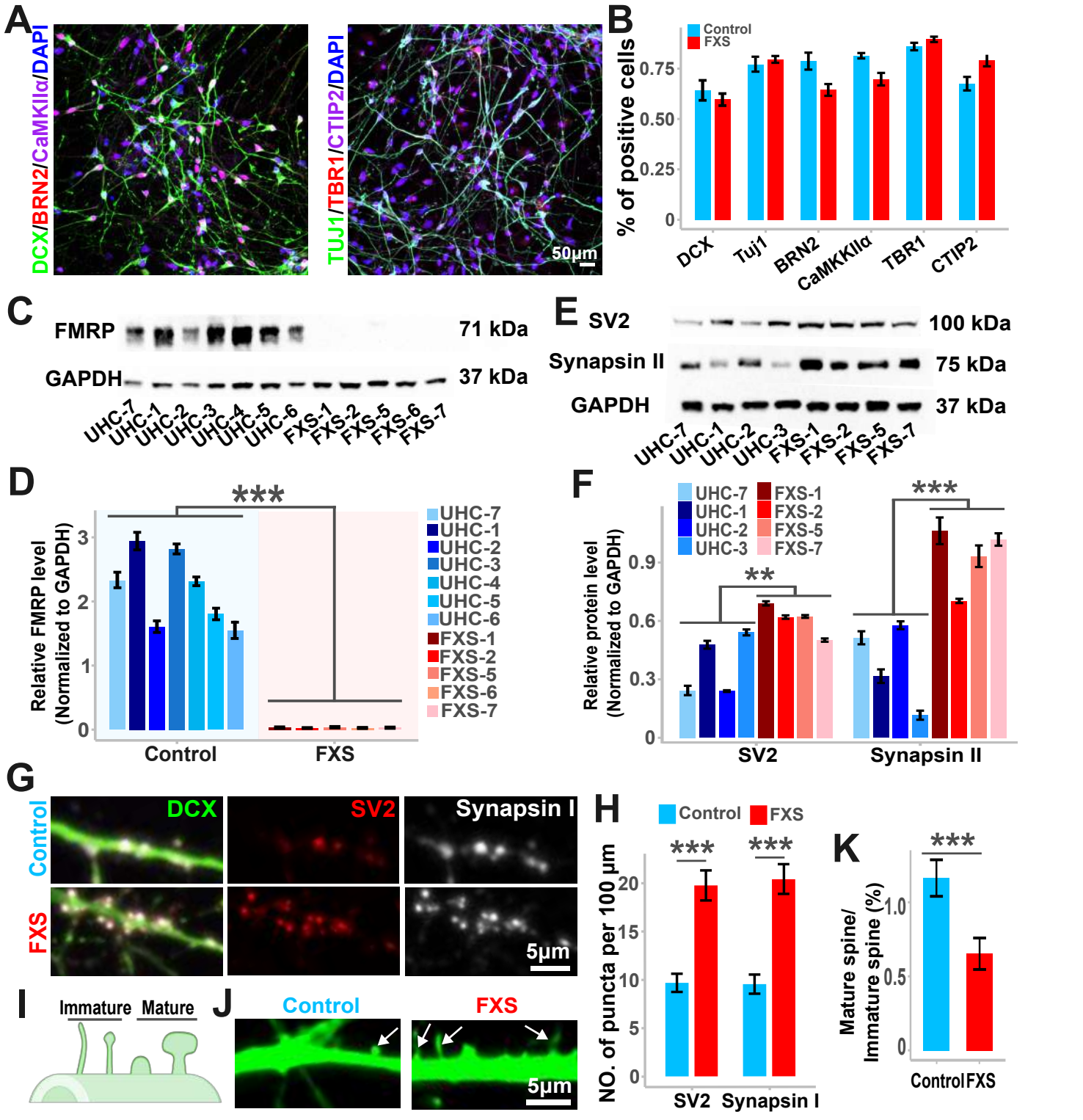

Figure 1. (Lu, et al.)

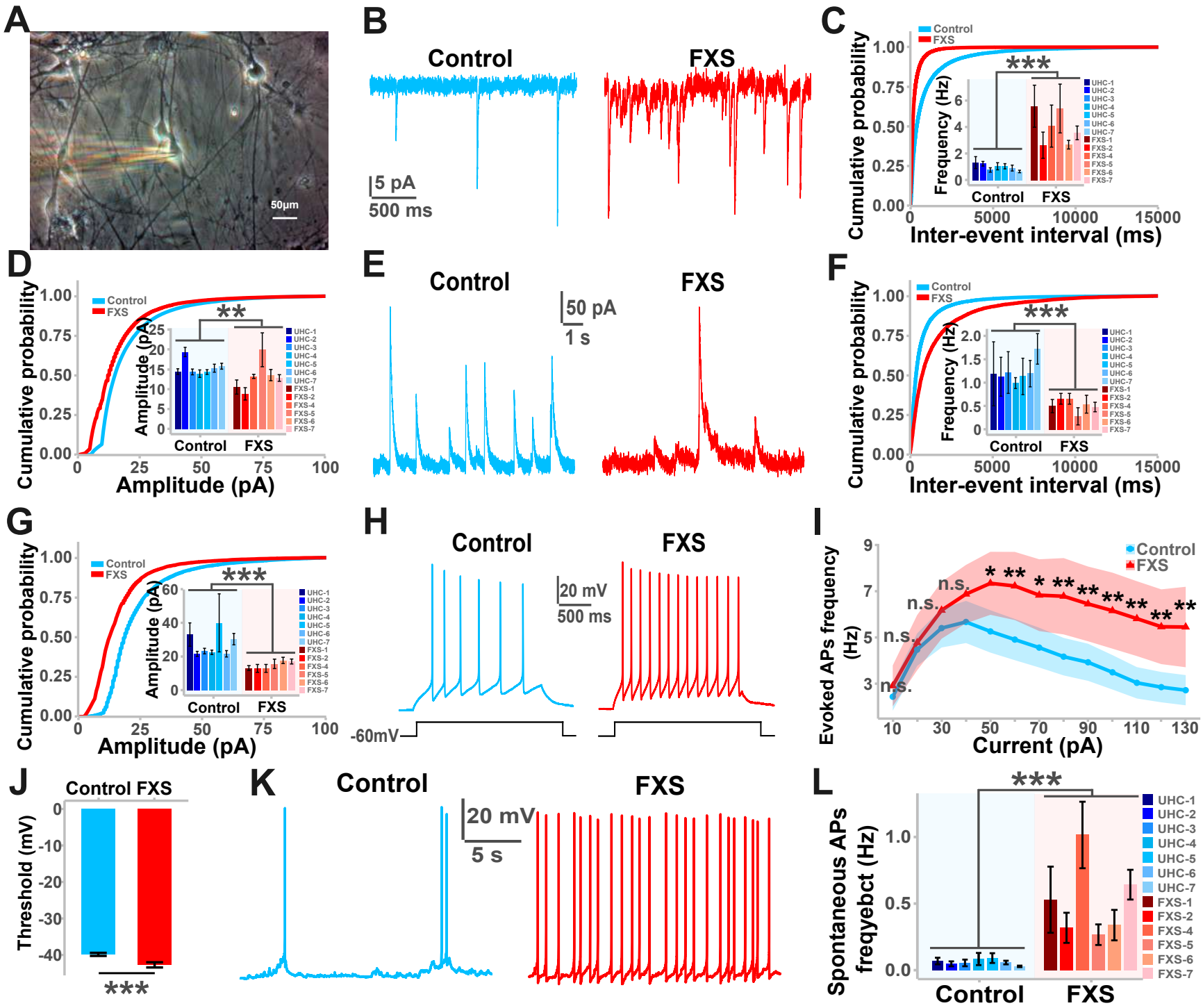

Figure 2. (Lu, et al.)

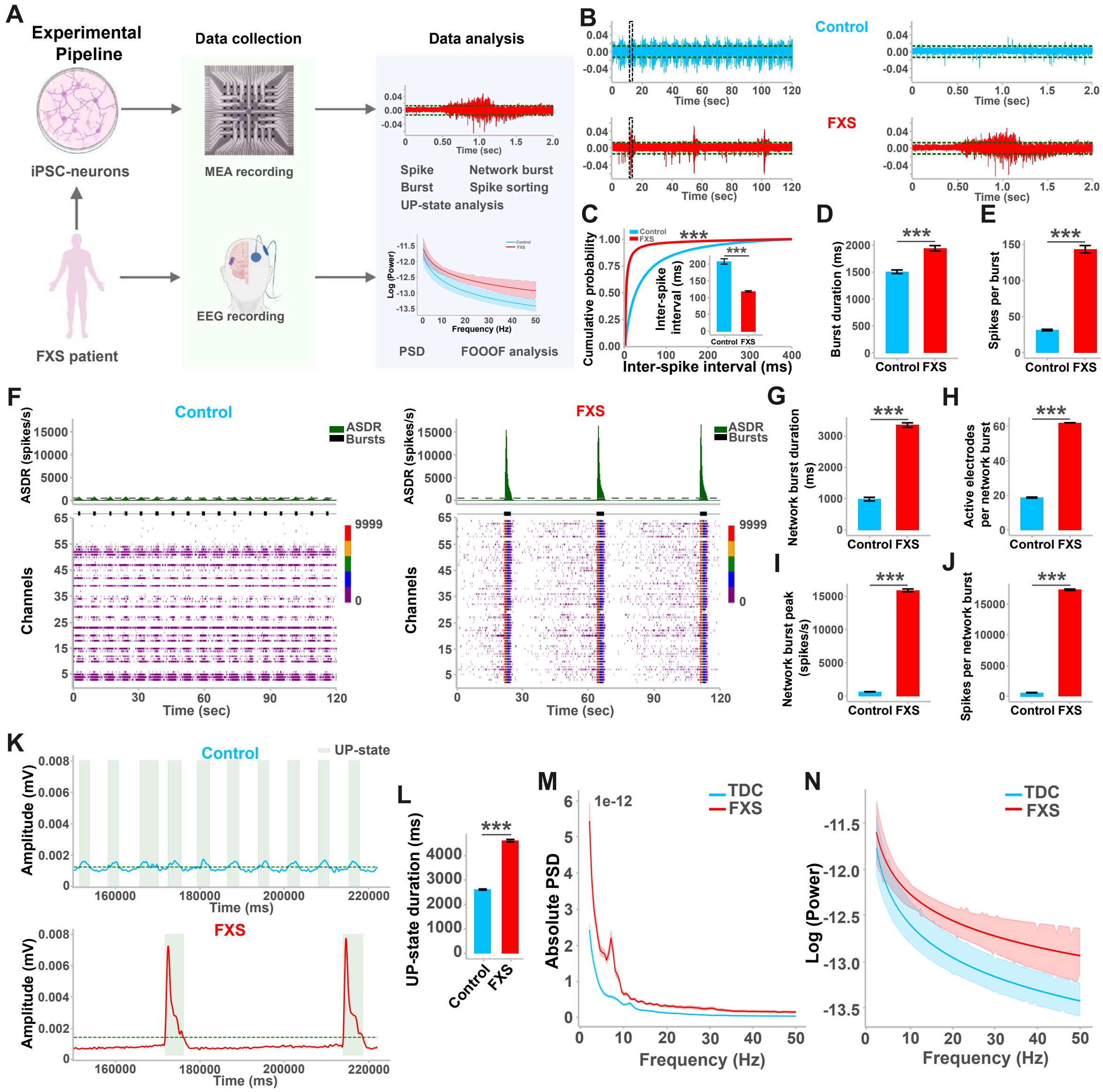

Figure 3. (Lu, et al.)

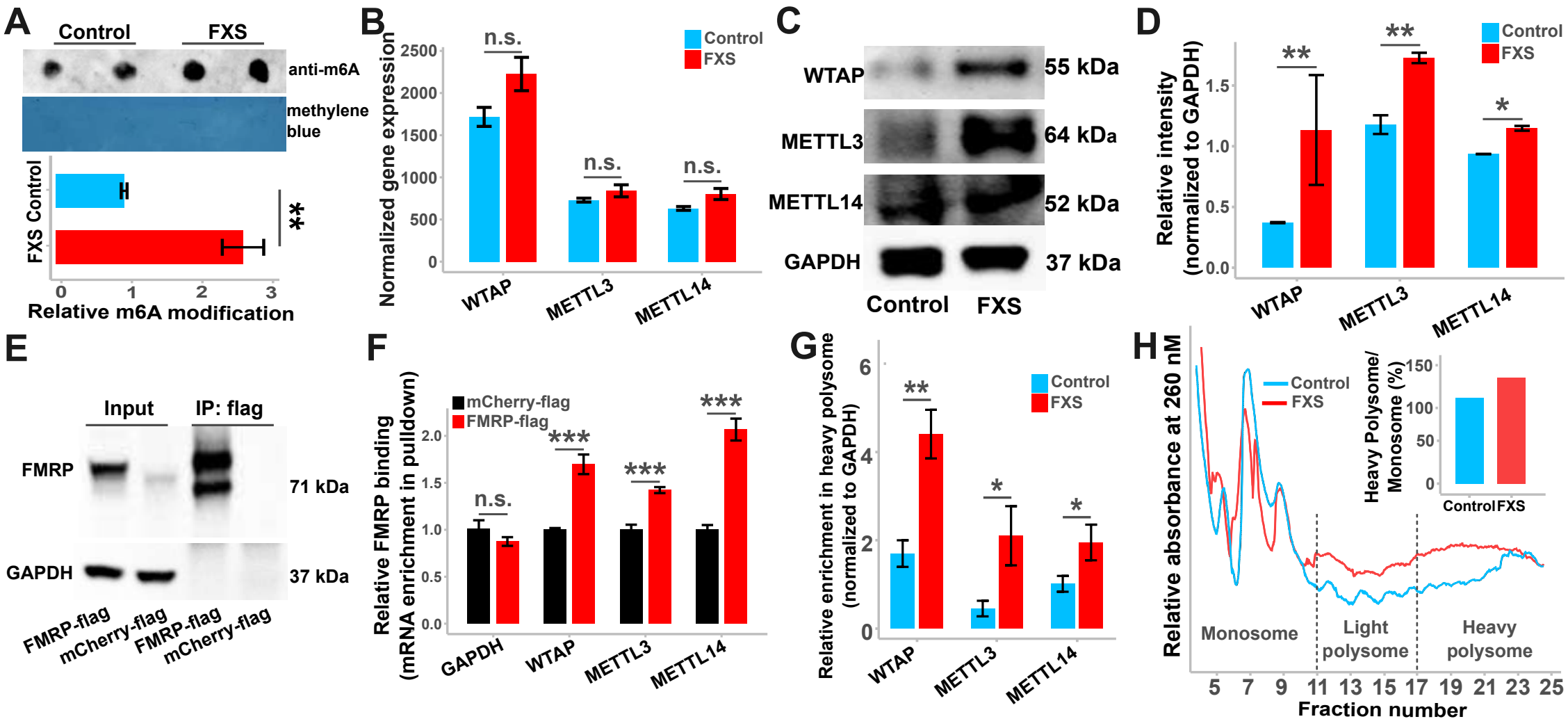

Figure 4. (Lu, et al.)

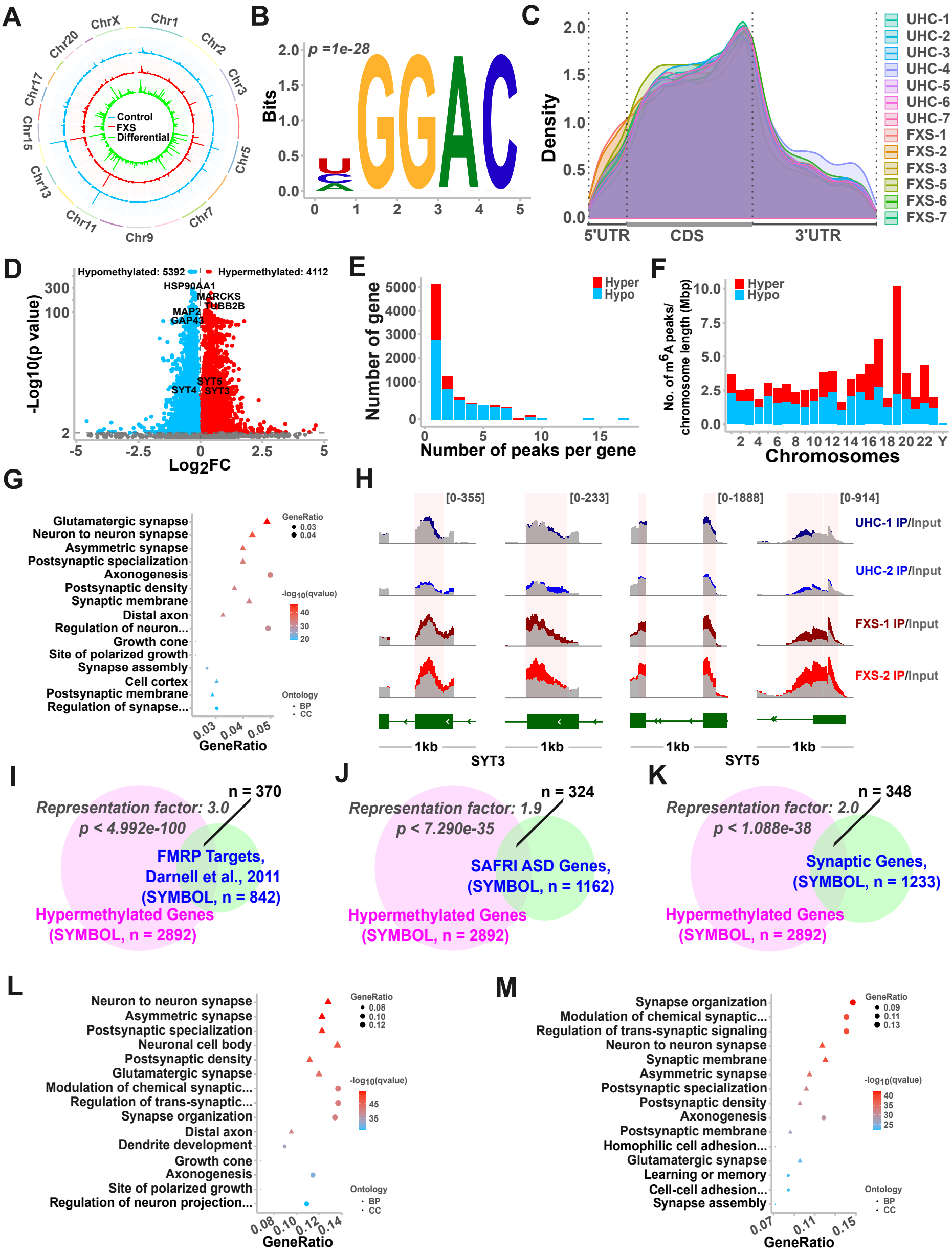

Figure 5. (Lu, et al.)

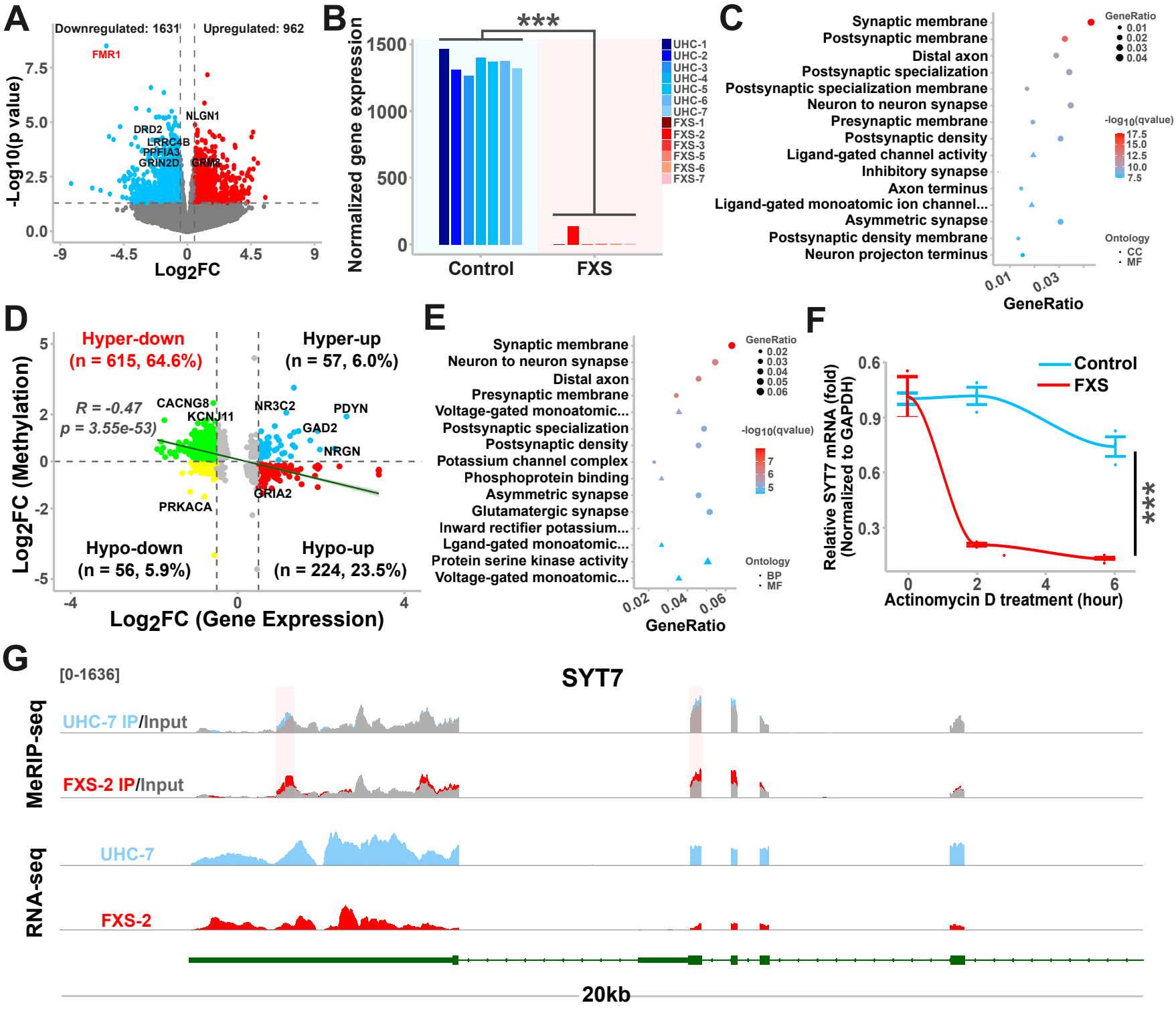

Figure 6. (Lu, et al.)

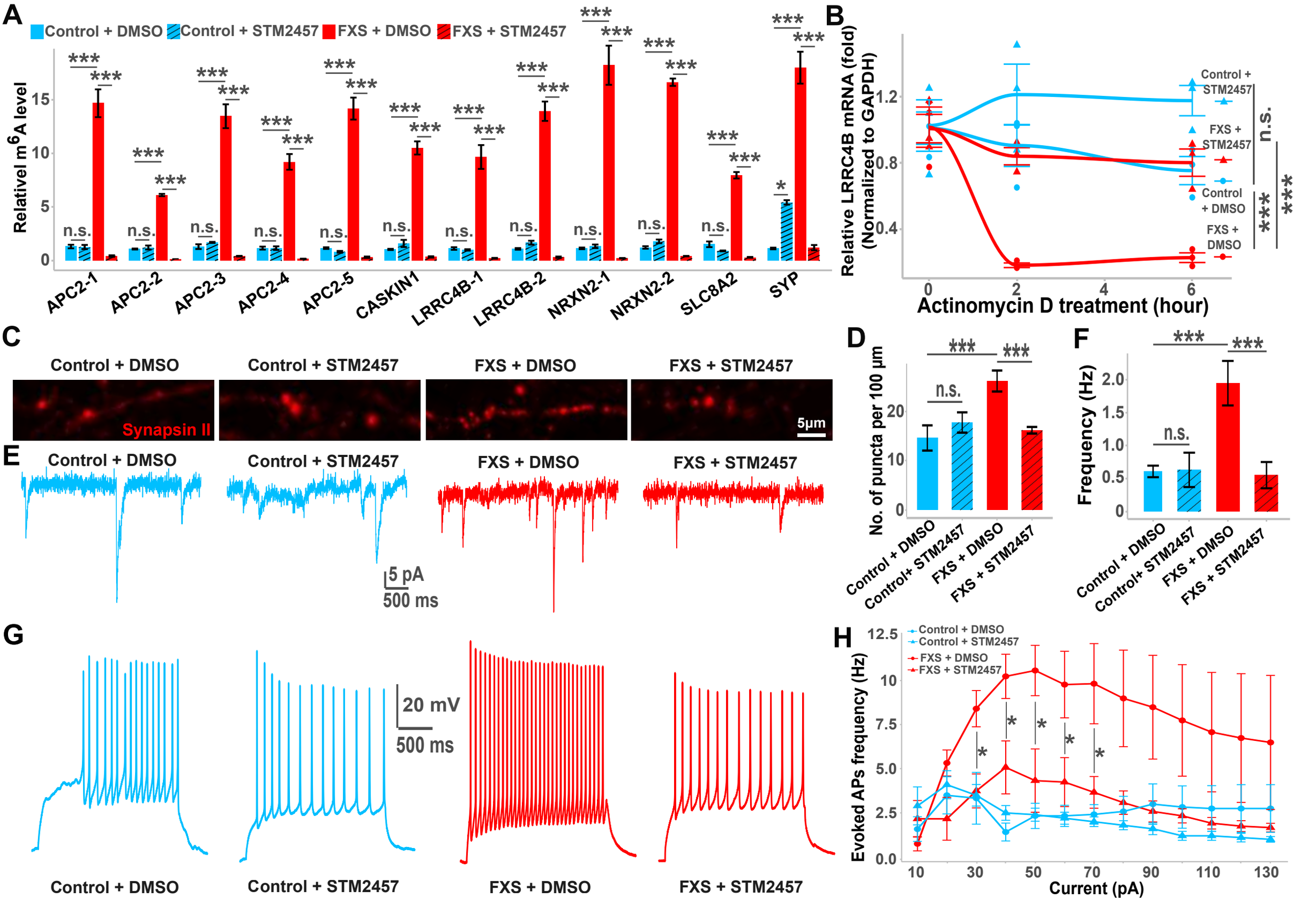

Figure 7. (Lu, et al.)